TECHNISCHE
UNIVERSITÄT
WIEN

Diploma Thesis

Phase-based RFID Localization Platform

performed at the

Institute of Electrodynamics, Microwave and Circuit Engineering
at
TU Wien

supervised by

Assoc. Prof. Dipl.-Ing. Dr. techn. Holger Arthaber
and
Univ. Prof. Ing. Dipl.-Ing. Dr.-Ing. Christoph Mecklenbräuker

by

Thomas Michael Pohl, BSc
Matr. Nr. 01328856

Vienna, August 24, 2022

Abstract

Radio Frequency Identification (RFID) technology has many professional applications, for example, in the fields of manufacturing, logistics, transportation, and the health sector. Cost-effective identification of people and objects has become an essential part of manufacturing processes. Since the identification process of RFID tags provides more situation-specific data than just a bare identification number, one may exploit this data to estimate the location of tagged people and objects.

For localization applications, the Ultra High Frequency (UHF) RFID technology is an appealing technology. Although not providing the localization accuracy of Ultra-Wideband (UWB) systems, it offers reasonable accurcy at much lower implementation costs. As UHF RFID tags are compact, only cost a few cents, and do not require batteries due to being powered from the reader, those tags are considered an optimum choice for applications with millions of tags or with disposable tags.

Several localization techniques for UHF RFID tags are known, e.g., phase-based, Received Signal Strength Indicator (RSSI)-based, or Angle of Arrival (AoA)-based. As the vast majority of algorithms do not consider the tags' movement as a parameter, the localization accuracy is inferior to expensive UWB systems. In order to gain comparable performance, one needs to put much more research in advanced algorithms, e.g., by considering a tag's possible movement trajectory.

For creating a high accuracy localization system in pharmaceutical clean rooms, this thesis focuses on developing a measurement platform to acquire the tags' phase information by multiple reader antennas. The measurement platform is the basis for obtaining precisely timestamped RFID tag measurements, which will be subsequently used in further development of algorithms with probabilistic Machine Learning (ML).

For the platform, I used a commercially available RFID reader from Kathrein Solutions GmbH with additionally added hardware to make reading on up to 16 antennas possible. This hardware also provides more accurate timing information than the RFID reader itself, which is essential for precise localization of moving tags.

Kurzfassung

Die RFID Technologie hat viele industrielle Anwendungen, z.B. in den Bereichen Fertigung, Logistik, Transport und Gesundheitswesen. Die kosteneffiziente Identifizierung von Personen und Objekten ist zu einem wesentlichen Bestandteil von Fertigungsprozessen geworden. Da der Identifizierungsprozess von RFID-Tags mehr situationsspezifische Daten als nur eine bloße Identifikationsnummer liefert, kann man diese Daten nutzen, um die Position der getaggten Personen und Objekten zu bestimmen.

Für Lokalisierungsanwendungen stellen UHF RFID Systeme eine vielversprechende Technologie dar. Sie bieten zwar nicht die Lokalisierungsgenauigkeit von UWB Systemen, erzielen aber eine brauchbare Genauigkeit bei wesentlich geringeren Herstellungskosten. UHF RFID Tags haben eine kompakte Bauweise, sind um wenige Cent herzustellen und benötigen keine Batterien, da sie vom RFID Lesegerät drahtlos mit Leistung versorgt werden. Somit gelten diese Tags als optimale Wahl für Anwendungen mit Millionen von Tags oder Einwegtags.

Im UHF RFID Bereich sind verschiedene Lokalisierungsverfahren bekannt, wie z.B. phasenbasierte, RSSI-basierte oder AoA-basierte Lokalisierung. Da die Mehrheit der existierenden Algorithmen die Bewegung der Tags nicht als Parameter berücksichtigt, ist die Lokalisierungsgenauigkeit von UHF RFID Systeme jener den teureren UWB-Systemen unterlegen. Um eine vergleichbare Leistung zu erzielen, muss man dabei viel mehr Forschung in fortschrittlichere Algorithmen investieren, z.B. durch Berücksichtigung der möglichen Bewegungstrajektorien der Tags.

Um ein präzises Lokalisierungssystem in pharmazeutischen Reinräumen zu schaffen, konzentriert sich diese Arbeit auf die Entwicklung einer Messplattform zur Erfassung der Phaseninformation der Tags durch mehrere Antennen. Die Messplattform ist die Grundlage für die Aufnahme präziser, mit hochgenauen Zeitinformationen versehener RFID Tag Messungen, die anschließend für die weitere Entwicklung von Algorithmen mit probabilistischem maschinellem Lernen (ML) verwendet werden sollen.

Für die Plattform habe ich ein kommerzielles RFID-Lesegerät der Firma Kathrein Solutions GmbH mit zusätzlicher Hardware erweitert, um die Messung an bis zu 16 Antennen zu ermöglichen. Diese Hardware liefert auch deutlich genauere Zeitinformationen als das RFID-Lesegerät selbst, was für die präzise Lokalisierung von bewegten Tags notwendig ist.

Acknowledgements

I want to thank all my colleagues and friends in the Microwave Engineering group at the Institute of Electrodynamics, Microwave and Circuit Engineering at TU Wien for their support. Special thanks to my professors Holger Arthaber and Christoph Mecklenbräuker for their constant support and inspiration.

This work was supported by the Christian Doppler Laboratory for Location-aware Electronic Systems.

Table of Contents

List of Figures

List of Tables

List of Abbreviations

AoA Angle of Arrival

CAN Controller-Area-Network

CEPT Conférence Européenne des Administrations des Postes et des Télécommunications

DC Direct-Current

DoA Direction of Arrival

DoD Direction of Departure

EIRP Equivalent Isotropically Radiated Power

EPC Electronic Product Code

ERP Equivalent Radiated Power

ETSI European Telecommunications Standards Institute

FCC Federal Communications Commission

FD Frequency Domain

FDX Full-Duplex

FSPL Free-Space-Path-Loss

GPIO General Purpose Input/Output

GUI Graphical User Interface

HCE Host-Card-Emulation

HF High Frequency

KRAI Kathrein RFID Antenna Interface

LF Low Frequency

LOS Line-of-Sight

ML Machine Learning

MUSIC Multiple Signal Classification

NFC Near-Field-Communication

NLOS Non-Line-of-Sight

PCB Printed Circuit Board

PDF Probability Density Function

PDOA Phase Difference of Arrival

PMI Polymethacrylimide

PoA Phase of Arrival

RCS Radar Cross-Section

RF Radio Frequency

RFID Radio Frequency Identification

RHCP Right-Handed Circular Polarization

RSSI Received Signal Strength Indicator

RX Receiver

S-Parameter Scattering Parameter

SD Spatial Domain

SEQ Sequential

SVM Support Vector Machine

TD Time Domain

TDoA Time Difference of Arrival

ToA Time of Arrival

ToF Time of Flight

UHF Ultra High Frequency

USB Universal Serial Bus

UWB Ultra-Wideband

VNA Vector Network Analyzer

WiFi Wireless Fidelity

1 Introduction

For identifying objects, Radio Frequency Identification (RFID) has become a widely used technology nowadays. These RFID systems are relatively cheap compared to Ultra-Wideband (UWB) systems for applications with millions of RFID tags. A working system consists of an RFID reader and at least one RFID tag. The reader acts as the interrogator that performs the transmission and reception of Radio Frequency (RF) signals, including the signal/data processing and decoding. The RFID tag is a rather small object, i.e., a sticker, with an antenna and electronics built-in. Fig. 1.1 shows a collection of some RFID tags used for test purposes in this thesis. They can be shaped as thin stickers, thicker and more robust plates, or tiny and flexible filaments. The larger tag at the bottom of Fig. 1.1 (MTP-110-K-A) is a multi-surface transponder. These tags are designed to be independent of the object's materials to which they are planned to be attached. Due to their robust construction, these tag models are suitable for harsh environments and metallic surfaces. RFID tags communicate with the RFID reader via backscatter modulation at a much lower power level.

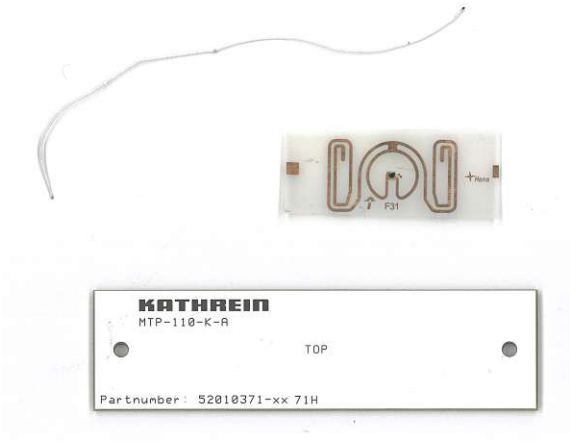

Figure 1.1: Collection of RFID tags

Dependent on the use case, RFID systems operate at different frequency bands. RFID systems in the Low Frequency (LF) band operate around 125 kHz, which leads to a short read range of approximately 10 cm with slow data rates. Today's typical RFID systems in the High Frequency (HF) band operate at around 13.56 MHz, for which the read range

rises to 50 cm, but also requires a large reader antenna for that range. The Near-Field-Communication (NFC) technology also uses this frequency band and relies on RFID protocols, with the main difference being its Host-Card-Emulation (HCE) capability, where the devices can act as readers or tags. Therefore, HCE makes two-way communication possible. This thesis uses the Ultra High Frequency (UHF) RFID band with reading ranges up to 10 m and much faster data rates. Today's production capabilities keep the costs for RFID tags low, which is an advantage over battery-powered UWB systems.

Before moving further, this part briefly summarizes the features of different RFID systems [1, p. 3]. Starting with the lowest frequency, typ. 125 kHz, the tags are primarily simple transponders and are read-only. These systems operate in Full-Duplex (FDX) mode. The second main system operates at around 13.56 MHz (NFC) with inductive coupling and read/write capabilities. The third part focuses on the UHF-RFID system, operating in the UHF band (865–868 MHz for Europe and 902–928 MHz for USA/Canada). This provides maximum read ranges of up to 10 m depending on the antennas and environment. Comparative to the LF system, UHF-RFID operates in Sequential (SEQ) mode instead of FDX mode. The data transfer from the tag to the reader typically works over backscatter modulation. Tab. 1.1 briefly summarizes the different technologies used in RFID systems. Since the UHF RFID version leads in all features of this table, the HF version seems to be obsolete. The HF band is used nowadays mostly for NFC applications, sometimes running Java applets with higher speeds and higher computational power, consuming higher amounts of energy. Additionally, one does not want high read ranges for all products, especially credit cards.

Frequency:	LF (< 1 MHz)	HF (13.56 MHz)	UHF (868 MHz/915 MHz)
Operation Mode	FDX	FDX	SEQ - state machine
Power Supply	active	passive	passive
Programmable	no	yes	yes
Range	< 1 cm	< 50 cm	< 10 m
Encryption	no	yes	yes

Table 1.1: Comparison of RFID systems

Focusing on the UHF RFID systems in Europe and USA, Conférence Européenne des Administrations des Postes et des Télécommunications (CEPT)/European Telecommunications Standards Institute (ETSI) and the Federal Communications Commission (FCC) are the authorities for band regulations. ETSI specifies 15 channels of 200 kHz, with a total bandwidth of 3 MHz from 865–868 MHz and a maximum power of 2 W Equivalent Radiated Power (ERP) [2]. For the US market, the FCC specifies 52 channels of 500 kHz each, with a total bandwidth of 26 MHz from 902–928 MHz and a maximum power of 4 W Equivalent Isotropically Radiated Power (EIRP). One should also differ between active and passive RFID systems. Active tags are battery-powered, while passive tags use the RF signal from the interrogator as their power supply.

When reading an RFID tag, one receives much more information than just the tag's Electronic Product Code (EPC), e.g., phase and Received Signal Strength Indicator (RSSI), and maybe some text data in the payload. One could use the additional information to make identification and localization possible. Existing methods use the phase, the RSSI, or both to compute position estimates.

Fig. 1.2 shows a typical channel model for passive RFID communication with two main paths. In this case, the Line-of-Sight (LOS) path will be the dominant one, but may drop if obstructions occur. Then, the Non-Line-of-Sight (NLOS) path, or reflected path may dominate. The RFID reader powers the tag in the so called forward link, and communication from the RFID tag to the reader is done via backscatter modulation, called reverse link. Since there is no battery in the RFID tag, the tag's answer to the reader will be at a low power level. This requires the reader to have high receiver sensitivity. Nevertheless, if there is enough power to supply the tag, the successful reception of its answer is usually not an issue.

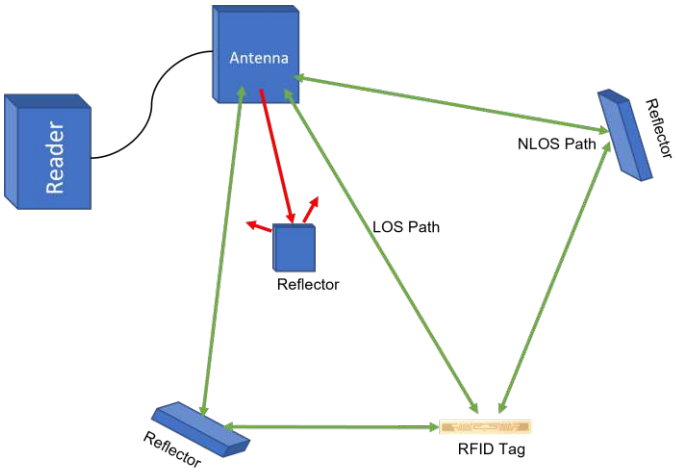

Figure 1.2: Typical RFID channel model

My used RFID system is based on the EPC Class-1 Gen-2 UHF RFID protocol, described in [3], and covers only passive RFID tags. Since using only RSSI information is too inaccurate in location estimation, I planned to use a phase-based approach with 16 antennas. Since there is no commercially available RFID reader with more than four antenna ports, the plan was to implement RF switches to multiplex the 16 antennas to the four antenna ports. The used RFID reader is a commercially available unit (RRU4500) from Kathrein Solutions GmbH with four antenna ports and a General Purpose Input/Output (GPIO) port for further external sequencing. In an RFID system, choosing suitable antennas is not a trivial question. Therefore, I did a few comparisons and used standard Right-Handed Circular Polarization (RHCP) antennas with two different radiation patterns. To get data from real-world scenarios, this measurement platform was set up in a room at the university.
This thesis focuses on constructing the measurement platform, the hardware, and the multiplexing concept. The first chapter introduces the theory of selected distance measurement methods and an overview of some existing localization methods. After that, I briefly introduce my concept for the measurement platform and the used hardware. The chapter covering the hardware describes the used RFID reader, the antennas, and additional developed hardware. The whole system is controlled and tested by self-created software, which is described with "How-To" guides in the appendices. The last chapters cover characterization, accuracy, and test measurements to calculate the resulting Angle of Arrival (AoA).

2 Theory and Related Work

To clarify the measurement platform's concept, I want to look at some existing distance estimation and localization methods first. These can be broadly separated into methods based on ranging, i.e., measuring the distance by RSSI and phase information, and techniques based on models simulating the dynamics of the scenarios and remembering known positions corresponding to specific values of RSSI and phase, known as fingerprinting methods.

There exist several publications of distance measurement and localization approaches. A good survey on the different methods of range-based and system modeling is given in [4]. The author of [5] shows position estimation by superimposing a weak, broadband spread-spectrum signal upon the RFID carrier signal. With a new mathematical technique, the author can separate the tag's response from the other echoes in the room.

There is also a recently published Ph.D. thesis on RFID localization techniques [6]. The author covers a localization method for UHF RFID tags with planar apertures generated by robotic arms that move the reader's antennas. Furthermore, this thesis investigates simulations on localization errors for different techniques based on digital beamforming. The second central part of this thesis deals with developing a localization system based on robotic arms' movement of an antenna array. The author aims to create a 3-dimensional map of the target space with the tagged objects. This system results in an average localization accuracy of 2.5 cm, which is promising, but the moving robotic arms are not easily usable in each environment.

The first section of this chapter covers common distance measurement methods based on the principle of Time of Flight (ToF), i.e., Phase of Arrival, Angle of Arrival, Time of Arrival, Time Difference of Arrival. The subsequent sections cover distance measurement and localization techniques utilizing the RSSI values, the fingerprinting method, and a short demonstration of the impact of multipath effects.

2.1 Time of Flight Methods

The basic principle for a ToF method is to measure the time difference between the transmission of a signal and its return to the receiver. Typical ToF methods for distance measurement use emitted light, e.g., laser, and capture the reflected one from one or more

objects. ToA, TDoA, PoA are some ToF methods covered in this section. Because all ToF methods require accurate timestamps and synchronized clocks, they will mostly not fit low power and low-cost solutions.

2.1.1 Angle of Arrival

AoA is a method to calculate estimates for directions by measuring angles. Looking at Fig. 2.1, we can see a typical scenario for angle measurements. We must have at least two or more antennas placed within a known distance to obtain this. We can then get the RFID tag's angle θ in (2.1) via the phase difference of the received signals at both antennas (φ_2 and φ_1) and the path difference $\Delta d = d_{\text{ant}} \sin(\theta)$. This method works well for angle estimation in clean environments under the assumption of a dominant LOS condition but suffers from multipath effects, which cause a reduction in accuracy. One should note that (2.1) holds for the tag's distance to the reader's antenna d_{ant} on antenna 1 being much larger than the spacing of the antenna pair d_{ant}; $d_{\text{ant}} \gg d_{\text{ant}}$.

$$\theta = \arcsin\left(\lambda \frac{\varphi_2 - \varphi_1}{2\pi d_{\text{ant}}}\right) \tag{2.1}$$

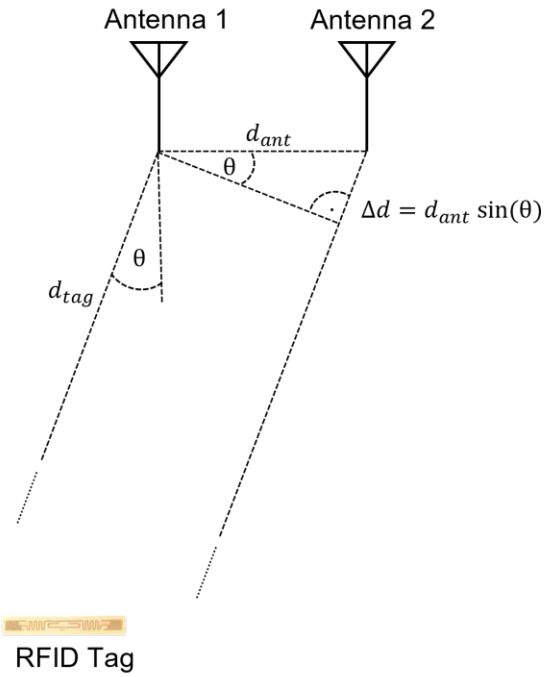

Figure 2.1: Model for AoA measurements

An AoA-based localization approach using UHF-RFID transponders is presented in [7] by evaluating the phase differences in their antenna arrays. Their self-designed antenna arrays consist of three elements each. These arrays can actively be switched to change the radiation pattern and, as a result, be able to follow multiple directions. This publication gives an attractive approach and good results with a mean deviation from the target of 0.21 m. The localization area is quite limited, at approximately 3 m × 3 m. Their concept is shown in Fig. 2.2.

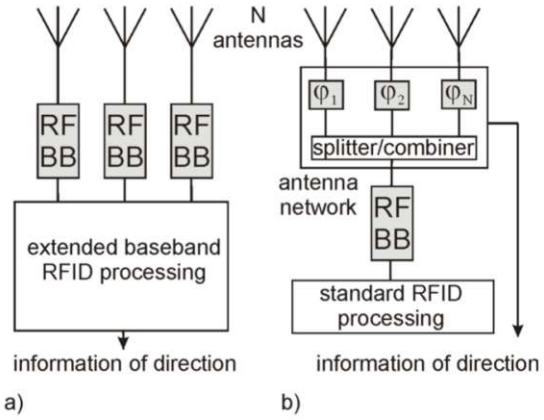

Figure 2.2: Concept for antenna arrays in [7]; a) digital beamforming, b) analog phase shifters; reprinted from [7, p. 92; Fig. 1.]

Another example uses Spatial Domain (SD) for localization estimation with an AoA approach [4]. Additionally, the publication also shows some angle measurements (Direction of Arrival (DoA), Direction of Departure (DoD)) with high accuracy but increased deployment costs due to the need for multiple antennas.

2.1.2 Time of Arrival

The ToA method belongs to the ToF methods with their assets and drawbacks. Publication [8, Ch. 14.7.4.1] presents a good example of a distance measurement with this method, which is shown in this section. Looking at the example with two terminals [8, Fig. 14.16; Ch. 14.7.4.1] in Fig. 2.3, one can obtain four different timestamps (t_1, t_2, t_3, t_4). In this example with two transceivers, i.e., terminals, t_1 marks the time for the first signal being sent by terminal 1, and t_2 the time the first signal has been received at terminal 2. The reverse path is from the time t_3 the terminal sends the answer, and t_4, where terminal 1 receives the answer from terminal 2. In Fig. 2.3, hatch patterned frames represent transmission and white frames represent reception at the respective terminals ([8, Fig. 14.16; Ch. 14.7.4.1]). The ToF for the current signal frame is declared as τ. Using the mean τ, one can then calculate the distance with (2.2)[8, (14.4); Ch. 14.7.4.1], by multiplying τ with the speed of light c. Since this method requires highly accurate and synchronized clocks for all terminals, which is expensive, it is not the first choice to start in this thesis' project. Another major problem using this method would be the supply and wiring of many base stations.

$$d = \tau \cdot c = \frac{(t_4 - t_1) - (t_3 - t_2)}{2} \cdot c \tag{2.2}$$

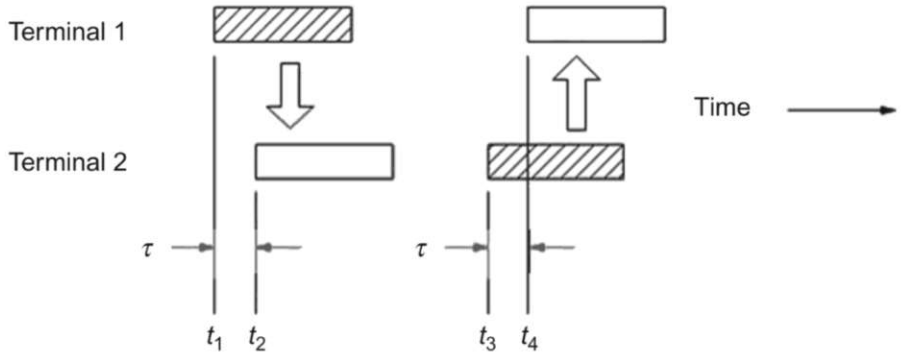

Figure 2.3: Distance estimation via ToA methods; reprinted from [8, Fig. 14.16; Ch. 14.7.4.1]

2.1.3 Time Difference of Arrival

TDoA measures the time difference between N antennas/base stations and a reference station. This is the main difference to ToA, not needing more than a single base station for distance measurement. Of course, for localization with triangulation methods, multiple base stations/antennas are required. The estimated location then lies at the intersection of hyperboloid functions. A good example of this method is shown in [9]. Fig. 2.4 shows this illustration of TDoA localization with a reference station and two additional stations with the localized target.

Equations (2.3) and (2.4) calculate the distances from the target to the particular base or reference station. The coordinates (x_i, y_i, z_i) refer to the position of the base station i, and (x, y, z) denote the target's position. The authors of [9] also consider a noise term n_i, described by the underlying assumptions of the random signals from the stations. The TDoA for base station i can then be calculated as shown in [9] and (2.5). The joint Probability Density Functions (PDFs) for the random signals are defined as independent zero-mean Gaussian processes. These assumptions can also be used for the ToA method but have less influence on simple distance measurements than 3-dimensional location calculations. One gets a system of equations with an equation for each node's $TDOA_{i,ref}$. By solving this equation system, one can calculate a solution for the target's position. Since this method also relies on highly accurate timing information, which is expensive, it is unsuitable for deployment in a low-cost concept.

$$\rho_i = \sqrt{(x - x_i)^2 + (y - y_i)^2 + (z - z_i)^2} \tag{2.3}$$

$$\rho_{ref} = \sqrt{(x - x_{ref})^2 + (y - y_{ref})^2 + (z - z_{ref})^2} \tag{2.4}$$

$$TDOA_{i,ref}\Big|_{ref=1} = \frac{1}{c_0}(\rho_i - \rho_{ref}) + n_i \tag{2.5}$$

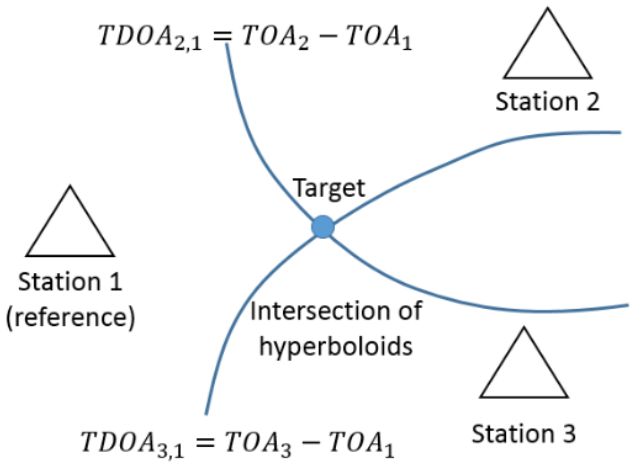

Figure 2.4: Illustration of TDoA localization; reprinted from [9, Fig. 2, p. 2]

This basic concept for TDoA is also known as the hyperbolic localization algorithm.

2.1.4 Phase of Arrival

PoA is another distance measurement method, which belongs as ToA and TDoA to the ToF methods. The main difference to the previously mentioned methods is that the relevant information is in the relative phase values of the transmitted and received signals. As shown in the following figure and equations from [8, Ch. 14.7.4.3], the distance d can be calculated with the speed of light c_0, assuming free space conditions and the phase θ $[0, 2\pi)$. The variable d_λ in (2.6) from [8, Ch. 14.7.4.3, (14.7)] is the distance indicated by the number of wavelengths λ between both transmitting devices.

$$d = \frac{c_0}{f}\left(\frac{\theta}{2\pi} + d_\lambda\right) \tag{2.6}$$

The publication [4] summarizes three types based on the Phase Difference of Arrival (PDOA): Time Domain (TD), Frequency Domain (FD), and SD. For the TD-PDOA, they concluded that it is not suitable for the situation of a moving tag at high velocities due to the phase periodicity. Distance estimation via FD-PDOA is done by measuring the tag phase at different frequencies. This frequency diversity leads to an increased localization accuracy compared to previous methods.

2.2 Received Signal Strength Indicator

Using the RSSI values, one can obtain a distance estimation by calculating the path loss. Therefore, we need to consider the transmitter power, the transmitter antenna gain, the RFID tag's antenna gain, and, of course, the radiation patterns of the participating antennas. One should note at this point that the RFID tag's antenna pattern is often unknown and hence makes RSSI values unpredictable. Equation (2.7) states the Frii's transmission formula, which is the ratio of received P_{RX} and transmitted power P_{TX}, consisting of the product of the antenna gains G_{TX}, G_{RX}, the wavelength λ, and the distance d between sender and receiver.

$$\frac{P_{\mathrm{RX}}}{P_{\mathrm{TX}}} = G_{\mathrm{RX}} G_{\mathrm{TX}} \left(\frac{\lambda}{4\pi d}\right)^2 \tag{2.7}$$

The squared last part in (2.7) can be formulated as the Free-Space-Path-Loss (FSPL) in (2.8).

$$L_{\mathrm{FSPL}} = \left(\frac{4\pi d}{\lambda}\right)^2 \tag{2.8}$$

Using the FSPL from the link budget, one can estimate the distance by (2.9).

$$d = \frac{\lambda}{4\pi}\sqrt{L_{\mathrm{FSPL}}} \tag{2.9}$$

This model works well in optimum LOS scenarios but suffers from multipath effects and obstructions. Fig. 2.5 shows two scenarios for the RSSI measurements. Fig. 2.5a would be a good scenario where no obstacles are present, and both antennas are facing in the optimum direction. Of course, the multipath effect is not considered here, which would worsen measurements. Fig. 2.5b shows a poor scenario where the main beam lobes are not facing each other. One needs to note in Fig. 2.5b, that the "poor" scenario is poor for an unknown tag's antenna pattern, which is mostly the case. Other effects to consider are the nonlinear change of the RFID tag's Radar Cross-Section (RCS) and the tag not being stationary, i.e., rotating/moving tag. The RCS value indicates how likely the desired objects can be detected and calculated under consideration of the tag's material, the size, the shape, and the antenna polarization of the target. Together with movements and

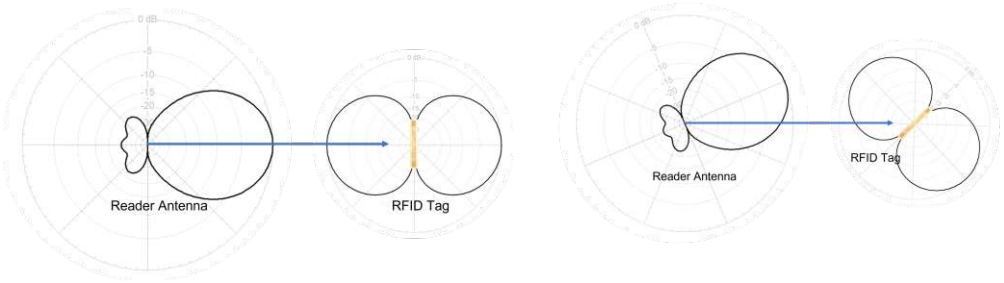

(a) (b)

Figure 2.5: Scenarios for RSSI measurements; a) good, b) poor (for unknown antenna pattern)

multipath effects, these changes in good and poorer scenarios can happen relatively fast and unpredictably, reducing the overall informative value of the RSSI. Therefore, the RSSI method is not the first choice for developing localization algorithms.

Some examples of this method can be found in [10] and [11]. The approach in [11] is not related to RFID, but they propose an alternative approach by estimating the AoA of the signal paths using only the autocorrelation of the magnitude of the received signals in the 5 GHz Wireless Fidelity (WiFi) band. Their results show approximately 30 cm tracking error for passive moving objects.

2.3 Fingerprinting Method

Distance estimation by using only RSSI values is not consistent and accurate for environmental changes due to multipath effects. The fingerprinting method aims to provide a unique position estimate for an RFID tag by reading the tag's RSSI values from multiple antennas and multiple positions, and comparing these values with saved ones in a lookup table in a database. One can use various further localization methods with the data from the database. Still, most publications cover the nearest neighbor location method [8].
The method of fingerprinting can be broken down into three main stages. In the first stage, the database must be filled with values for all detectable RFID tag's RSSI values and the corresponding real position in the defined grid. This can be done with motorized positioners to precisely move the RFID tags in a defined grid with known resolution. The second stage involves recording the RSSI values from all antennas/receivers. This stage is also called the "online" phase since the system actively records the live RSSI values for all detected RFID tags. In the third stage, the measurement data from the second stage are compared to those reference values in the database. The final location is calculated from the data of the closest recorded RSSI value. Fig. 2.6 shows an example of this method.

The publication [12] describes a classification algorithm for a UHF RFID system. Their approach uses K-Nearest Neighbors and curve-fitting algorithms for distance estimation and the RSSI values as fingerprints. To find the nearest neighbor, they compare the current measured RSSI values to those stored in the database in different frequencies. Their resulting localization accuracy is at 18.3 cm.
Publication [13] describes a UHF RFID localization algorithm based on Machine Learning

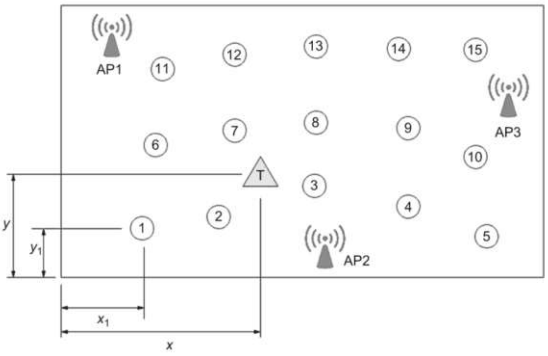

Figure 2.6: RFID fingerprint method for location estimation; reprinted from [8, Fig. 14.15, p. 411]

(ML) to transform the problem of localization into a classification problem. Instead of using the RSSI values for localization, the authors used outputs from their Multiple Signal Classification (MUSIC) algorithm as fingerprints to obtain higher accuracy and more robustness to multipath scenarios. Since they use classification algorithms with their area divided in segments, the localization accuracy depends on the size of the segments. This work presents a localization accuracy of 0.23 m^2 segment size with 97 % detection probability. Generally, several methods in the fingerprinting segment are combined with other measurement and ML-based methods, e.g., combining RSSI data with RCS and database models in [14]. These techniques can deal with all kinds of ML methods, like Kalman filtering in [15] or by using Support Vector Machines (SVMs) [16]. Fig. 2.7 shows the data collection from [13] in segments. The black dots in their visualization represent the originally placed RFID tags. The colors represent the readability of the tags in the segments, where the red ones were invisible due to destructive interference. The orange segments represent the areas where the tags were read just a few times in comparison to the white segments, where the tag could be read most of the overall measurement time.

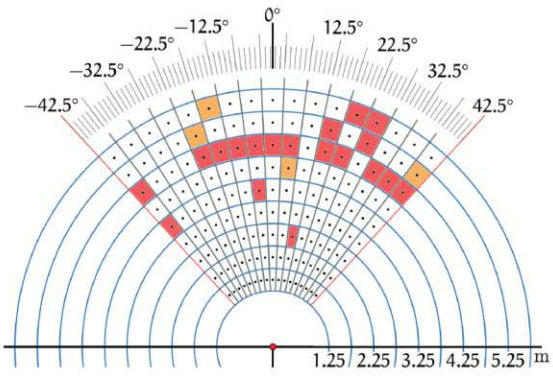

Figure 2.7: Data collection results in segments; reprinted from [13, Fig. 3, p. 209]

2.4 Impact of Multipath Effects

Since nearly all localization methods suffer from multipath effects, one needs to find a way to resolve each channel. Looking at Fig. 2.8, one can see samples with multipath propagation and LOS path for different bandwidth pulses. In Fig. 2.8a the multipaths cannot be differentiated, so one can see only some flat fading for this narrowband system (< 1 MHz). This expresses the behavior for the UHF RFID system, which has 200 kHz of channel bandwidth for ETSI regulations. For Fig. 2.8b (10 MHz bandwidth) and Fig. 2.8c (100 MHz bandwidth), one can already see a better resolution but some significant signal distortions and fading effects. Fig. 2.8d shows a more accurate resolution using a UWB pulse of 1 GHz to see the LOS signal. This shows the high bandwidth requirement for ToF measurements, relying on precise timestamps demonstrating the need for a UWB system to resolve the multipaths accurately. Since an RFID system has only about 200 kHz of bandwidth in an ETSI regulated UHF RFID channel, the solution with a UWB system is not directly applicable.

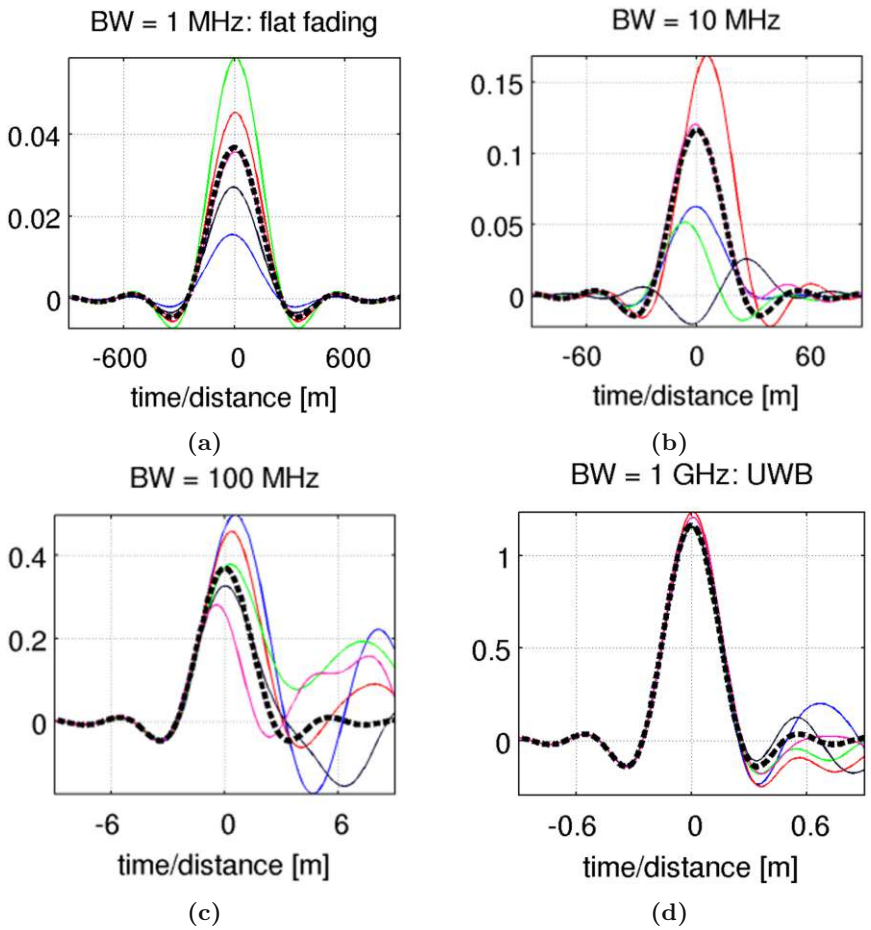

Figure 2.8: Impact of multipath on ranging; a) 1 MHz BW, b) 10 MHz BW, c) 100 MHz BW, d) 1 GHz BW; (Legend: —— multipath sample 1, —— multipath sample 2, —— multipath sample 3, —— multipath sample 4, —— multipath sample 5, - - - LOS); reprinted from [1, Slide 10]

3 Measurement Platform

This chapter is about developing the measurement platform, necessary hardware, and additional devices for reference and positioning. The first section will describe the top-level design with the overall antenna placements and combinations. The second section is about the controller design and the interface to Matlab. Lastly, this chapter shows some additional hardware developed for precisely determining the antenna locations relative to the distance measurement device, including the construction of linear axes for homing and reference movements of a tag with an exact known location.

I planned to use a phase-based approach for my measurement platform. Therefore, I used a commercially available RFID reader from Kathrein Solutions GmbH with four antenna outputs. Since I wanted to use 16 antennas in the system, and there is no commercially available RFID reader with more than four antenna outputs, the available ports from the Kathrein RFID reader were multiplexed achieving antenna diversity. Another reason to use the RFID reader from Kathrein was the GPIO port for sequencing of external hardware. The unit has two Ethernet ports, making deployment and communication easy. To achieve the 16 antennas for the setup, I used solid-state RF switches and built a controller that synchronizes with the reader to operate the RF switches correspondingly.

For the test setup, I built this measurement platform in a room at the university. One should note that this measurement platform focuses both on moving and static objects. This thesis follows up on two main scenarios in my concept. The first focuses on detection in the whole room, and the second focuses on more precise detection in workplaces.

Considering ETSI regulations for Europe and the 865–868 MHz band, the RFID reader uses channels 4 (865.7 MHz), 7 (866.3 MHz), 10 (866.9 MHz), and 13 (867.5 MHz) with a bandwidth of 200 kHz for each channel. By changing the channels alternatively during the measurement process, frequency diversity can be achieved with this system.

Fig. 3.1 shows a block diagram for the concept of the measurement platform. This includes the RFID reader from Kathrein and four RF switches to multiplex the available antenna ports to a maximum of 16 antennas. Depending on the local requirements, one can easily change the antenna type at each port. A reference tag exists at the last port of the fourth RF switch to record dynamic influences to the phase, which are not related to movements of RFID tags.

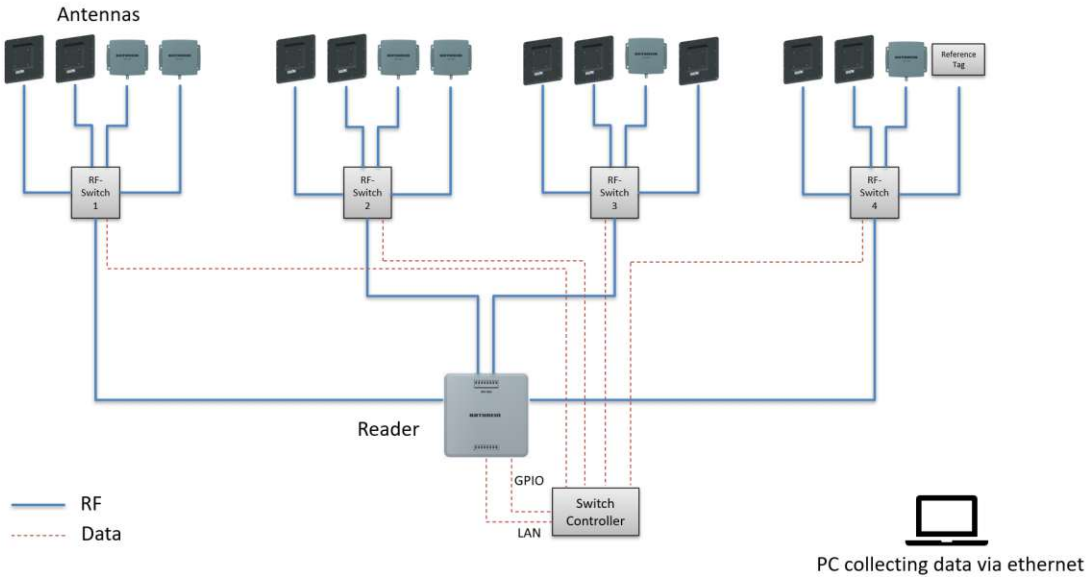

Figure 3.1: Block diagram for the concept of the measurement setup

3.1 RFID Reader

Generally, one can use any UHF RFID reader unit that fits the requirements of high transmit power, low receiver sensitivity, and as many antenna output connectors as possible. To quickly get the possibility to experiment with these systems, I used a commercially available RFID reader unit from Kathrein in the ETSI configuration. This unit, shown in Fig. 3.2, provides a maximum conducted power output per port of 33 dBm and typical −80 dBm Receiver (RX) sensitivity. It provides four antenna outputs, a GPIO port with four in-/outputs, and two Ethernet ports.

Figure 3.2: RFID reader unit RRU4500

The reader unit is restricted in the ETSI configuration to the 865–868 MHz frequency band, and is licensed to the standards: EN302208-2 V2.1.1, EN301489-3, EN50364, EN62368-1, EN60529, EPC Gen2 V2, UCODE DNA.
Tab. 3.1 shows the reader's communications profiles that can be set per software.
The RFID reader is capable of two central encoding schemes, "FM0" and "Miller". Both are described in the EPC Gen2 V2 standard [3]. FM0 is a bi-phase encoding scheme, where a logical 1 is indicated as a constant "High" or constant "Low" level in the bit's time window. A level transition in the center of the bit's timeframe indicates a logical 0 value. At each symbol end, the phase gets inverted for this scheme.
Compared to the FM0 encoding, for Miller encoding, a logical 1 is represented in the form of a "Low to High" or a "High to Low" transition. In contrast to the FM0 encoding, Miller encoding does not change the logical level for a logical 0 unless another logical 0 occurred previously. In this case, there will be a transition of the logical level. This Miller encoding scheme has a distinctive feature of modulated subcarriers. These subcarriers are used to achieve better reception of weak backscattered signals. For this scheme, the data bits are encoded in the baseband and then multiplied in frequency with the number of the sub-carrier, e.g., 2,4,8. This advantage comes at the expense of more used bandwidth.

Mod.	$R_{b,TX}$ [kbit/s]	$R_{b,RX}$ [kbit/s]
FM0	40	64
FM0	40	80
FM0	40	160
FM0	80	160
FM0	80	320
FM0	80	512
Miller2	40	80
Miller2	80	80
Miller2	80	160
Miller4	40	40
Miller4	40	64
Miller4	80	40
Miller4	80	160
Miller8	80	40

Table 3.1: RRU4500 communication profiles

For my test measurements, I used the communication profile 9, featuring "Miller2" modulation with $R_{b,TX} = 80\,\text{kbit/s}$ and $R_{b,RX} = 160\,\text{kbit/s}$. This decision for the "Miller2" encoding is based upon the advantages of Miller encoding of more robust communication and subsequent higher read rates than with FM0 modulation.

3.2 Antennas

Theoretically, one can use any antenna that matches the corresponding reader requirements. Since Kathrein sells various types, it was apparent to look at their antenna models. For the platform, I was looking for some small antennas for workplaces and antennas with higher gain for detection in the room. The model type WRA7070 fits the room detection scenario, and the MIRA-100 fits the workplace detection. The wide-range antenna (WRA) types can be purchased in Kathrein RFID Antenna Interface (KRAI) configuration and as standard RHCP antennas.

KRAI is a technology by Kathrein for communicating with the antennas and make active antenna functions possible, e.g., switching to different antenna polarizations, custom LED functions on the antenna, or cascading antennas for Kathrein's smart shelf antenna models. This KRAI protocol transmits at 22 kHz with a supply voltage of 5 V, superimposed onto the RF signal. I did several investigations on some antennas with KRAI functionality but decided to use passive antennas only. KRAI protocol provides many additional functions but turned out to slow down the read rate and is not possible to use for my setup since it requires a DC power supply via coax cable, which is not possible to run via the solid-state RF switches. These considerations led me to use nine pieces of WRA7070 antennas in combination with six mid-range antennas of type MIRA-100.
The WRA7070 and MIRA-100 are both RHCP antennas with an impedance at the antenna port of 50 Ω in the 865–868 MHz band. The WRA7070 model has an antenna gain of approximately 8.5 dBiC, and the MIRA-100 has approximately 2.5 dBiC.

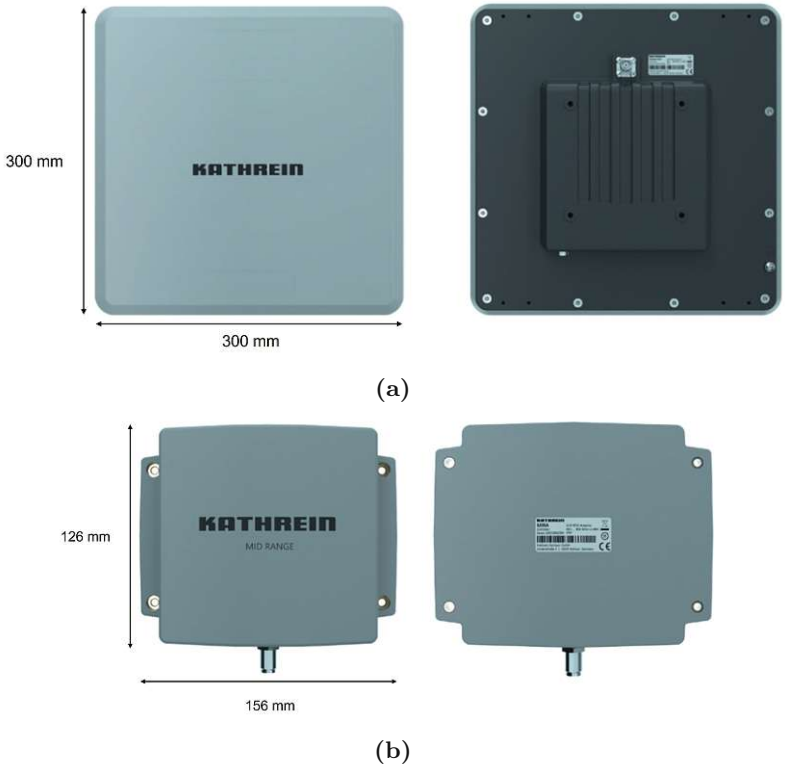

Figure 3.3: Antenna models: a) WRA7070 (wide-range antenna); b) MIRA-100 (mid-range antenna)

3.3 Controller

The main task for this controller is to operate each of the switches, synchronize with the reader unit, and communicate with the Matlab interface software. At each inventory round of the RFID reader unit, the controller should switch all four RF switches to the next configured position. The power supply for this unit is generated using the +24 V from the GPIO port of the RFID reader which is converted via DC/DC converters to the necessary 3.3 V for the RF switches and 5 V for the processor. The core of this controller is an Arduino Nano V3. Ethernet communication to the controller is implemented using an XPort converter from Lantronix. This device acts as a Serial-to-Ethernet converter and communicates with Arduino via a software serial port. Connection to the switches is set up via four standard 9-pin D-Subminiature connectors. Each RF switch has three digital pins to control the output, which need to be set as written in the truth table in the manufacturer's manual. The schematic for the controller is shown in Appendix A.

I designed the schematic as well as the Printed Circuit Board (PCB) in Autodesk EAGLE. The size of the 2-layer PCB is approximately 160 mm × 100 mm. An additional "Trigger" port provides debugging capabilities, and the Universal Serial Bus (USB) port is for flashing the firmware to the processor. Fig. 3.4 shows the front view and Fig. 3.5 shows the back view of the controller with its connectors.

Figure 3.4: RF switch controller front view with 9-pol D-Sub connectors to the RF switches

For synchronization with the RFID reader unit, the GPIO features of the reader were investigated first. The reader provides four input and four output pins, which can be set to different functions per software command. Several tests showed that the most reliable option for GPIO synchronization is to use the RF-On function. This function switches a selected GPIO pin if the RFID reader turns its RF power on. This signal is then fed to an input of the Arduino to operate the switches according to a selected antenna configuration.

Four SP4T solid-state RF switches from Mini-Circuits of model number ZSWA4-63DR+ are used to switch the four antenna ports from the reader to 16 antennas. These switches

Figure 3.5: RF switch controller back view with GPIO, USB and Ethernet connectors

provide excellent isolation (57 dB up to 2.7 GHz), linearity (IP3 +58 dBm at 1.9 GHz), high switching speed (320 ns), and can handle up to +33 dBm of power.

3.4 Test Area

To test the measurement platform and to get real-world data, the platform operates in a room with approximately 6 m × 5.2 m × 4 m (length, width, height) at the university. The WRA7070 antennas are used in the four top corners for room detection, and MIRA-100 antennas act as near-field antennas for workplace detection. The large WRA7070 antennas are placed in pairs to be able to do test measurements on AoA methods. The small, near-field antennas on one side of the room are also used in pairs, while on the other workplaces, a mixture of near-field and wide range antennas will be in use for close range detection. To get a universally applicable system to mount all the antennas at a certain height, I built a frame of traverse parts. Fig. 3.6 shows a photo of the room with the RFID reader and antennas highlighted. Fig. 3.7 shows a top view of the measurement room No. CF0135 at our institute at the university. On the top is the window side, and at the bottom is the entrance door to the room. The whole traverse system in this figure is blue, which is at a height of approximately 3 m above the floor. The structure to lift the platform to this height is in the four corners, also marked blue and built using traverses. The WRA7070 antenna models are orange, and the MIRA-100 antenna models are cyan. The RFID reader unit, marked in red, sits in the center of the traverse bar connecting both sides. Since I only have four cables for the RFID reader with a length of 6 m, the reader needs to be placed in the center of the room to avoid different cable lengths to the RF switches.

Figure 3.6: Measurement Room from the door side

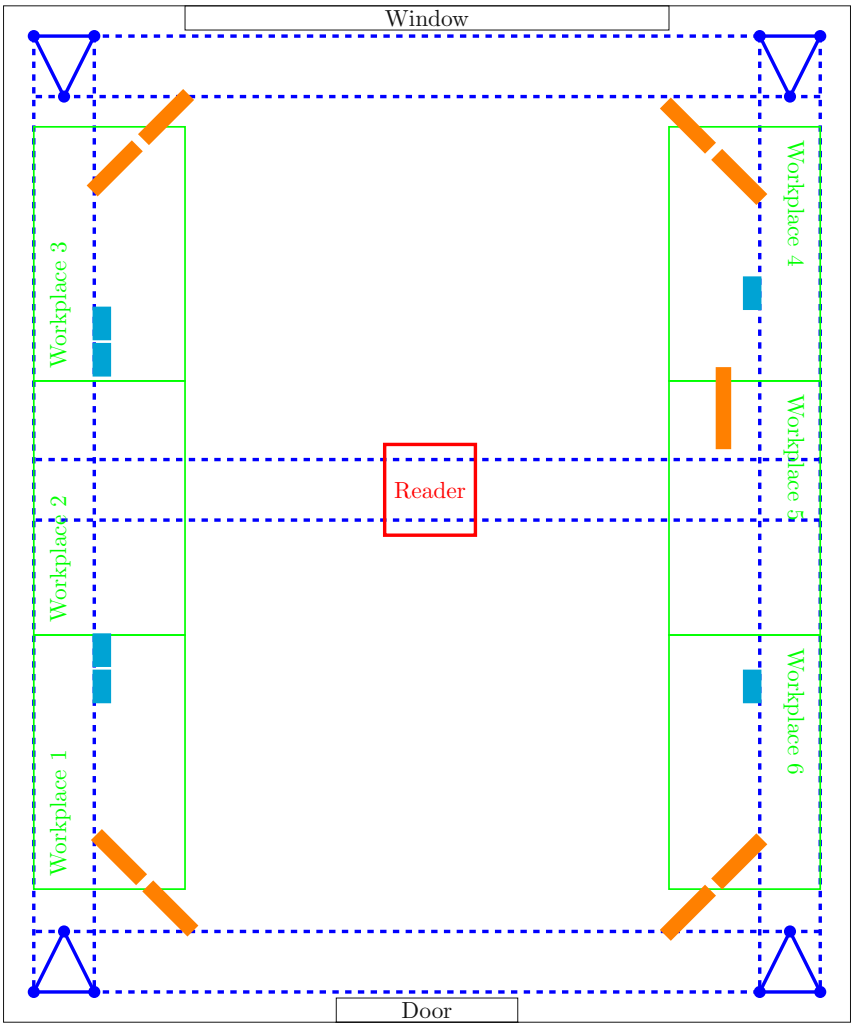

Figure 3.7: Top view of the measurement room No. CF0135; Elements: trussing system, RFID Reader (Kathrein RRU4500), workplaces / tables, WRA7070, MiRa-100

3.5 Matlab Interface

The implemented Matlab interface is the overall controller for the RFID reader unit and the RF switches in this measurement platform. It connects to the RFID reader and the RF switch controller via Ethernet, allowing easy hardware deployment, manages RFID reading commands, and stores the detected RFID tag information. Matlab classes were created for both devices to make elementary communication possible. The operation can be done smoothly via an implemented Graphical User Interface (GUI). Right after the start, the Matlab interface sets up Ethernet connections to the RFID reader and the controller and does initialization routines on both devices. On the RFID reader, the initialization routine consists of all setup and user-specific settings. These handle the RF power on the ports, the GPIO input and output functions, the user profile, and the initial value for the Q value. The user profile for the RFID reader specifies the bit rate and the data encoding for the communication between the reader and the tag. The initial value that needs to be set for the Q value is important to be set corresponding to the number of RFID tags that lie in the antenna's range and need to be detected. This number of maximum expected RFID tags is sent to the RFID reader as 2^Q. This Q value is communicated to the tags. Based on that, the RFID tags select a random slot in the communication to the RFID reader. Since I want the efficiency to be as high as possible, most of these timeslots in the communication should be occupied, and, of course, no packet collisions should occur. If the RFID reader detects a too large Q value, it will adjust this over time. On the controller for the RF switches, the initialization routine is quite different from that of the RFID reader. This consists of time synchronization with the interface and the user-selected antennas' settings. Since the RFID reader gives a too inaccurate timestamp on each detected tag, which is just in the accuracy of seconds, another source for more accurate timing information was necessary. Based on this requirement, the controller synchronizes the clock with the interface in its initialization routine. When both devices have finished their initialization, they are ready to receive inventory commands. An inventory command tells the RFID reader to scan for RFID tags. Each RF pulse on an antenna port on the reader switches the corresponding GPIO function to instruct the switch controller. At each GPIO pulse, the controller knows the current time relative to the start synchronization and sends the current timestamp for the corresponding GPIO pulse to the interface. Subsequently, the interface can calculate accurate time stamps for the detected tags in millisecond accuracy. For the case of multiple detected tags in a timeframe of a single RF-On pulse, the interface calculates the individual timestamps to be uniformly distributed. Fig. 3.8 shows a demo view of the GUI to control the Matlab interface. After the script finishes, it outputs a Matlab struct for further data processing. Fig. 3.9 shows a demo output, containing the relevant data fields, i.e., the EPC, frequency, phase, RSSI, timestamp, main and sub port. The main port numbers represent the four available antenna ports on the RFID reader, and the sub ports specify the four output ports on each RF switch.

A full description and a "How-To Guide" on the control sequence of the RF switch controller and the interface operation is included in Appendices C and D.

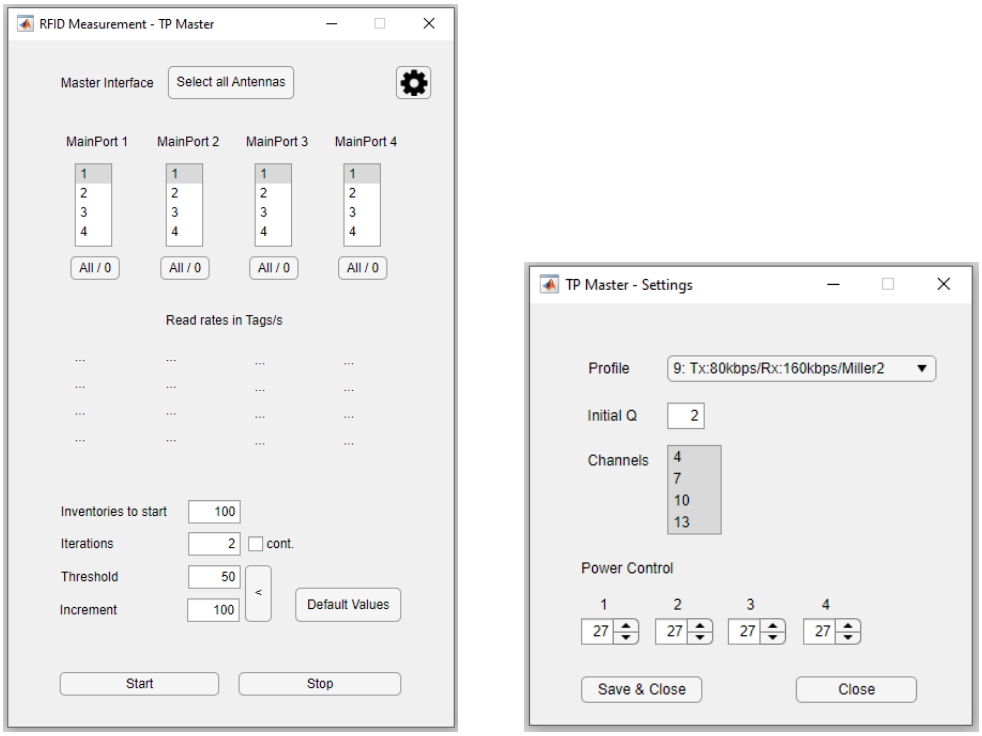

(a) **(b)**

Figure 3.8: Matlab GUI for the interface; a) Main interface, b) Settings window

Fields	EPC	Frequency	Phase	RSSI_dBm	NewTime	MaiP	SubP
1	"E2C0 6912 0000 003A 1E9A 15AA"	865700	-11.2000	-77.9700	"13-04-2022 13:09:23.287"	1	1
2	"3034 F459 8004 DEC0 0000 0001"	865700	-84.2000	-83.9900	"13-04-2022 13:09:23.333"	1	1
3	"E2C0 6912 0000 003A 1E9A 15AD"	865700	-270	-77.9700	"13-04-2022 13:09:23.399"	3	1
4	"E2C0 6912 0000 003A 1E9A 15AA"	865700	-303.6000	-80.2500	"13-04-2022 13:09:23.420"	4	1
5	"E2C0 6912 0000 003A 1E9A 15AC"	865700	-39.2000	-64.6900	"13-04-2022 13:09:23.421"	4	1
6	"E2C0 6912 0000 003A 1E9A 15AD"	865700	-292.4000	-78.6700	"13-04-2022 13:09:23.440"	1	2
7	"E2C0 6912 0000 003A 1E9A 15AA"	865700	-45	-70.1500	"13-04-2022 13:09:23.448"	1	2
8	"E2C0 6912 0000 003A 1E9A 15AC"	865700	-185.6000	-65.9300	"13-04-2022 13:09:23.493"	4	2
9	"E2C0 6912 0000 003A 1E9A 15AA"	865700	-22.4000	-63.1100	"13-04-2022 13:09:23.512"	1	3
10	"3034 F459 8004 DEC0 0000 0001"	865700	-230.6000	-81.1700	"13-04-2022 13:09:23.536"	2	3
11	"E2C0 6912 0000 003A 1E9A 15AD"	865700	-191.2000	-64.1300	"13-04-2022 13:09:23.554"	3	3
12	"E2C0 6912 0000 003A 1E9A 15AC"	865700	-247.4000	-47.2300	"13-04-2022 13:09:23.572"	4	3
13	"E2C0 6912 0000 003A 1E9A 15AA"	865700	-264.2000	-70.1500	"13-04-2022 13:09:23.592"	1	4
14	"3034 F459 8004 DEC0 0000 0001"	865700	-303.6000	-77.3300	"13-04-2022 13:09:23.614"	2	4
15	"0109 AA20 0505 26AA 1125 31AA"	865700	-39.2000	-68.2100	"13-04-2022 13:09:23.667"	4	4
16	"E2C0 6912 0000 003A 1E9A 15AA"	865700	-16.8000	-77.3300	"13-04-2022 13:09:23.691"	1	1
17	"E2C0 6912 0000 003A 1E9A 15AA"	865700	-67.4000	-76.1700	"13-04-2022 13:09:23.726"	2	1
18	"E2C0 6912 0000 003A 1E9A 15AD"	865700	-303.6000	-77.9700	"13-04-2022 13:09:23.744"	3	1
19	"E2C0 6912 0000 003A 1E9A 15AA"	865700	-270	-80.2500	"13-04-2022 13:09:23.764"	4	1
20	"E2C0 6912 0000 003A 1E9A 15AC"	865700	-45	-64.6900	"13-04-2022 13:09:23.765"	4	1

Figure 3.9: Example output of detected tags

4 Characterization

This chapter is dedicated to testing the performance limits (e.g. phase, RSSI) of the RFID reader. The results provide information on the accuracy of the later used model for localization. The first parts in this chapter cover the hardware setup that is required to study the readers performance, and its characterization. The last part covers developed hardware and software to precisely measure distances, e.g., relative distances from antennas to tags.

4.1 Measurement Setup

For analyzing the RFID reader's accuracy of phase and RSSI measurements, I used a wired RFID tag in combination with an RF circulator, an RF coupler, an RF step attenuator and a phase shifter. The setup can be seen in Fig. 4.1. The forward path to the tag is realized by a single attenuator of 20 dB and the attenuation of the RF coupler of approx. 11 dB. The reverse path goes straight through the RF coupler to the combination of RF step attenuator and phase shifter, to the reader via the RF circulator. For calibrating the setup in the process of measurement, I split the RF step attenuator and phase shifter into a single 2-port, and the remaining parts into a 4-port system. In further processing, the Scattering Parameters (S-Parameters) are measured from the 2-port and 4-port separately to be able to investigate the reverse path in detail. To get to the resulting S-Parameters of the complete combined measurement system, I take advantage of Mason's gain formula (4.1). The following section describes the entire process of this method.

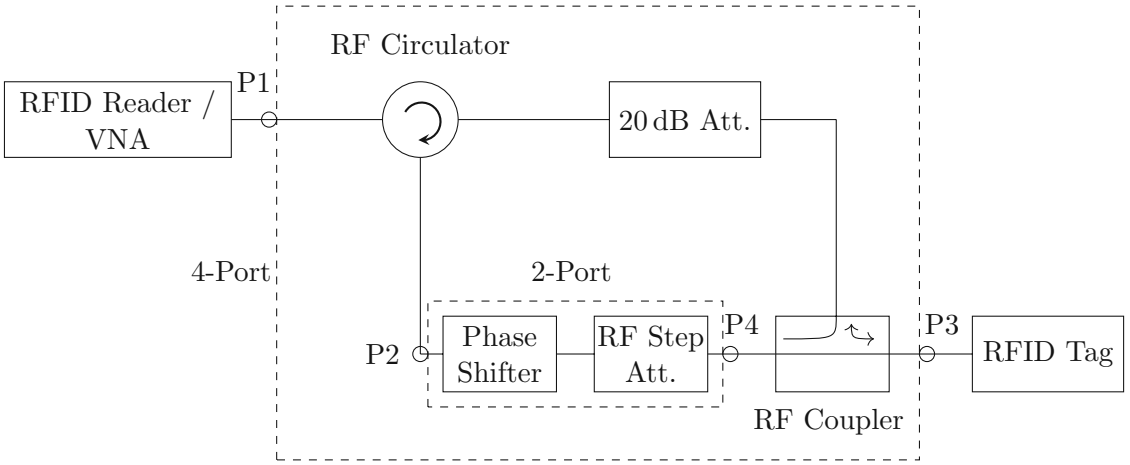

Figure 4.1: Setup for characterization of the RFID reader

4.2 Setup Characterization

The full measurement setup now separates into a 4-port and 2-port. Each is characterized by a set of S-Parameters. First, the S-Parameters of the 2-port, consisting of an RF step attenuator and a phase shifter, are measured with a Vector Network Analyzer (VNA). This measurement is acquired by a Matlab code, reading the data via Ethernet. Measurement of the S-Parameters for the remaining 4-port is done again with a VNA. To finally obtain a single 2-port, the two setups were connected together and the overall S-Parameters could be calculated. As mentioned previously, the idea was to use Mason's gain formula for the combination of S-Parameters which can be defined in (4.1) and (4.2) from [17].

$$T = \frac{\sum_{k=1}^{N} P_k \Delta_k}{\Delta} \tag{4.1}$$

$$\Delta = 1 - \sum G_{L_i} + \sum G_{L_i} G_{L_j} - \sum G_{L_i} G_{L_j} G_{L_k} + \dots \tag{4.2}$$

Equation (4.1) describes the total gain T of the system, P_k is the k-th forward path, and Δ_k is Δ minus the removed loop gains in Δ that touch the forward path k. The Δ in (4.2) is constructed as 1 minus the sum of the loop gain of any closed loop, plus the sum of the product of the loop gains of nontouching loop pairs minus the sum of the product of three pairwise nontouching loop gains. Equation (4.2) continues in an alternating form depending on the number of loops in the system. Fig. 4.2 shows the constellation.

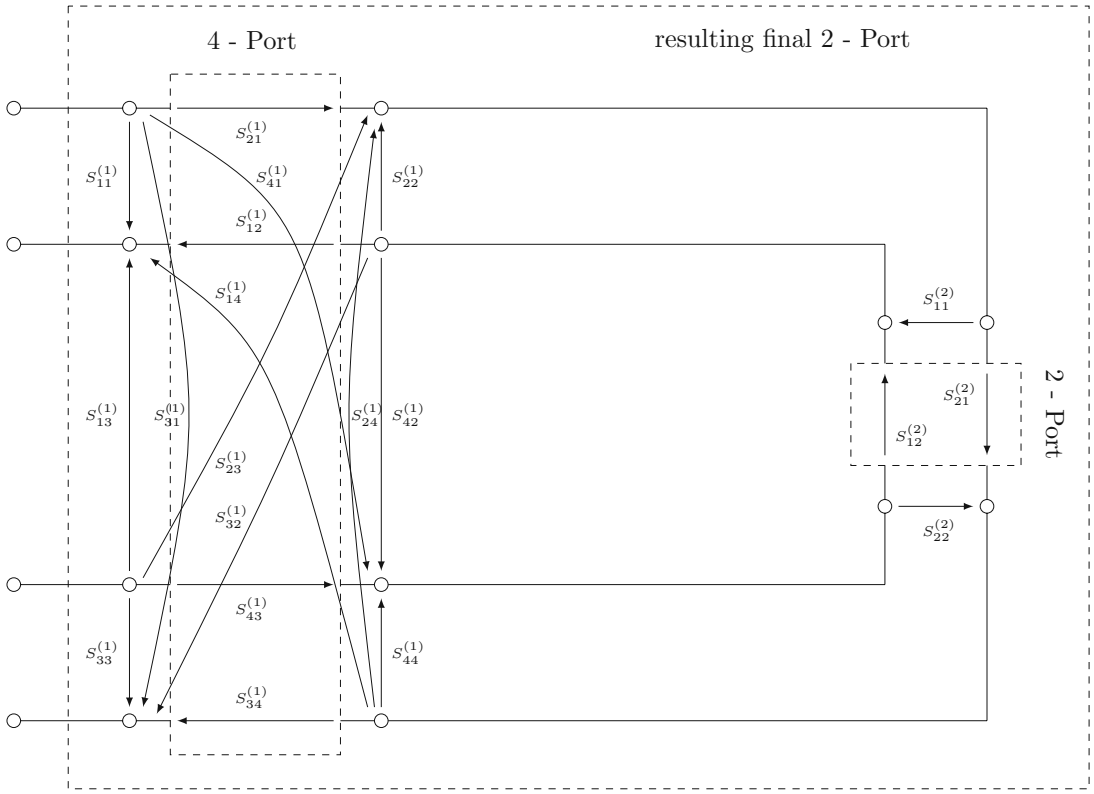

Figure 4.2: Setup constellation for the characterization process

4.2.1 S_{11} Total

Looking at Fig. 4.3, one can obtain the overall loops G_{L_i} $(i \in 1, 2, \ldots, 5)$ and the forward paths P_j $(j \in 1, 2, \ldots, 7)$ for the total S_{11}. Δ and Δ_k $(k \in 1, 2, \ldots, 7)$ are formed as described above. The loop gains G_{L_i} stay the same for each part of the total S-Parameters S_{11}, S_{13}, S_{31}, S_{33}. The green marked S-Parameters are participating in the current calculation. This procedure also repeats for the calculation of S_{13} total, S_{31} total, and S_{33} total.

$$G_{L_1} = S_{22}^{(1)} S_{11}^{(2)} \tag{4.3}$$
$$G_{L_2} = S_{22}^{(2)} S_{44}^{(1)} \tag{4.4}$$
$$G_{L_3} = S_{22}^{(1)} S_{21}^{(2)} S_{44}^{(1)} S_{12}^{(2)} \tag{4.5}$$
$$G_{L_4} = S_{42}^{(1)} S_{12}^{(2)} \tag{4.6}$$
$$G_{L_5} = S_{24}^{(1)} S_{21}^{(2)} \tag{4.7}$$
$$G_{L_6} = S_{22}^{(2)} S_{24}^{(1)} S_{11}^{(2)} S_{42}^{(1)} \tag{4.8}$$

$$P_{1,11} = S_{11}^{(1)} \tag{4.9}$$
$$P_{2,11} = S_{21}^{(1)} S_{11}^{(2)} S_{12}^{(1)} \tag{4.10}$$
$$P_{3,11} = S_{21}^{(1)} S_{21}^{(2)} S_{44}^{(1)} S_{12}^{(2)} S_{12}^{(1)} \tag{4.11}$$
$$P_{4,11} = S_{21}^{(1)} S_{21}^{(2)} S_{14}^{(1)} \tag{4.12}$$
$$P_{5,11} = S_{41}^{(1)} S_{12}^{(2)} S_{12}^{(1)} \tag{4.13}$$
$$P_{6,11} = S_{41}^{(1)} S_{22}^{(2)} S_{14}^{(1)} \tag{4.14}$$
$$P_{7,11} = S_{41}^{(1)} S_{12}^{(2)} S_{22}^{(1)} S_{21}^{(2)} S_{14}^{(1)} \tag{4.15}$$

$$\Delta = 1 - (G_{L_1} + G_{L_2} + G_{L_3} + G_{L_4} + G_{L_5}) + G_{L_1} G_{L_2} \tag{4.16}$$

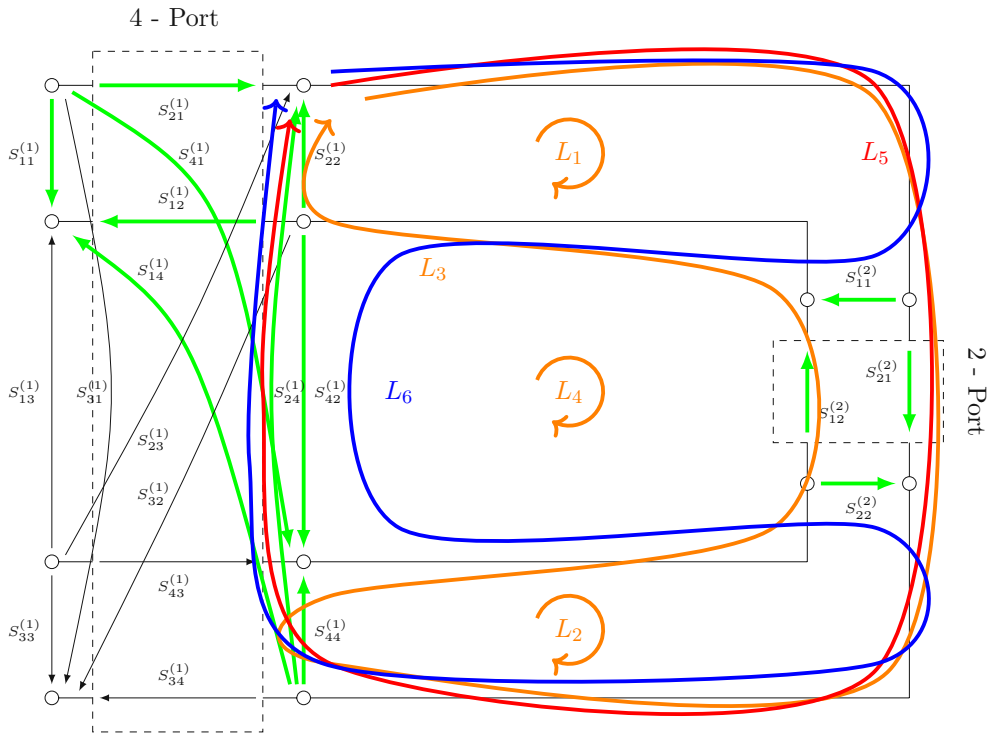

Figure 4.3: Setup constellation for the characterization process of S_{11} total

$$\Delta_{1,11} = 1 - (G_{L_1} + G_{L_2} + G_{L_3} + G_{L_4} + G_{L_5}) + G_{L_1}G_{L_2} \tag{4.17}$$
$$\Delta_{2,11} = 1 - G_{L_2} \tag{4.18}$$
$$\Delta_{3,11} = 1 \tag{4.19}$$
$$\Delta_{4,11} = 1 - G_{L_4} \tag{4.20}$$
$$\Delta_{5,11} = 1 - G_{L_5} \tag{4.21}$$
$$\Delta_{6,11} = 1 - G_{L_1} \tag{4.22}$$
$$\Delta_{7,11} = 1 \tag{4.23}$$

$$S_{11,\text{ total}} = \frac{1}{\Delta}\sum_{n=1}^{6} P_{n,11}\Delta_{n,11} \tag{4.24}$$

Equation (4.24) calculates the final total S_{11} of the 4-port by using the calculated loops and path gains in (4.3) to (4.23).

4.2.2 S_{13} Total

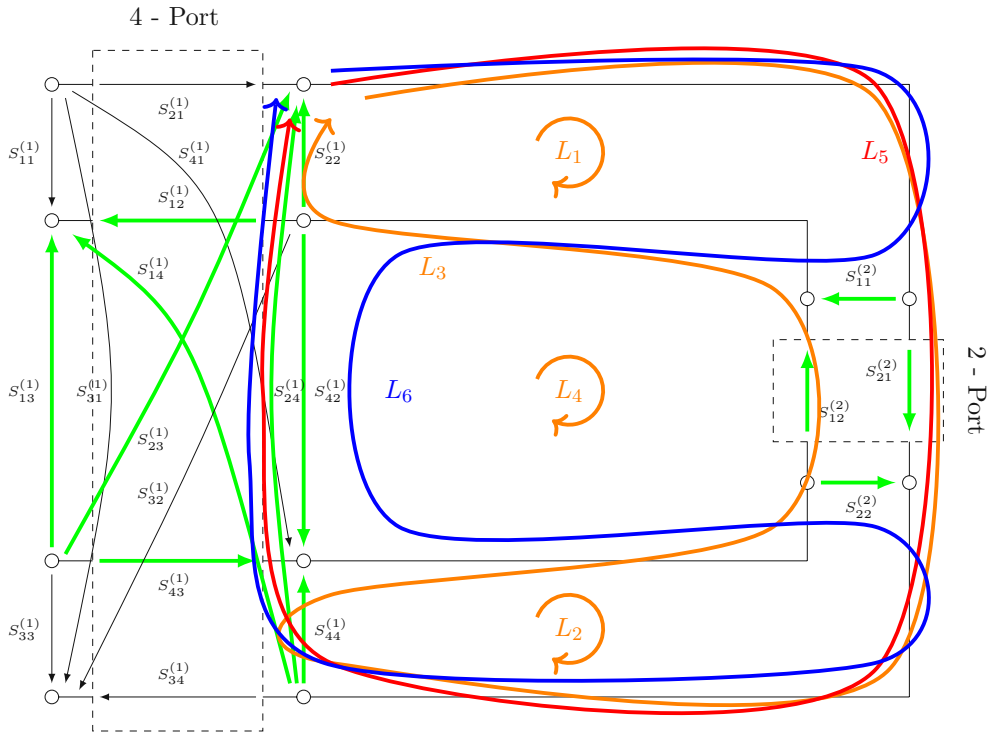

Figure 4.4: Setup constellation for the characterization process of S_{13} total

The total S_{13} is solved exactly with the same techniques as the previous part for S_{11}. The loops and the participating S-Parameters in this calculation are marked in color in Fig. 4.4.

$$P_{1,13} = S_{13}^{(1)} \tag{4.25}$$
$$P_{2,13} = S_{43}^{(1)} S_{12}^{(2)} S_{12}^{(1)} \tag{4.26}$$
$$P_{3,13} = S_{43}^{(1)} S_{22}^{(2)} S_{14}^{(1)} \tag{4.27}$$
$$P_{4,13} = S_{23}^{(1)} S_{11}^{(2)} S_{12}^{(1)} \tag{4.28}$$
$$P_{5,13} = S_{23}^{(1)} S_{21}^{(2)} S_{14}^{(1)} \tag{4.29}$$
$$P_{6,13} = S_{23}^{(1)} S_{21}^{(2)} S_{44}^{(1)} S_{12}^{(2)} S_{12}^{(1)} \tag{4.30}$$
$$P_{7,13} = S_{43}^{(1)} S_{12}^{(2)} S_{22}^{(1)} S_{21}^{(2)} S_{14}^{(1)} \tag{4.31}$$

$$\Delta_{1,13} = 1 - (G_{L_1} + G_{L_2} + G_{L_3} + G_{L_4} + G_{L_5}) + G_{L_1}G_{L_2} \tag{4.32}$$
$$\Delta_{2,13} = 1 - G_{L_5} \tag{4.33}$$
$$\Delta_{3,13} = 1 - G_{L_1} \tag{4.34}$$
$$\Delta_{4,13} = 1 - G_{L_2} \tag{4.35}$$
$$\Delta_{5,13} = 1 - G_{L_4} \tag{4.36}$$
$$\Delta_{6,13} = 1 \tag{4.37}$$
$$\Delta_{7,13} = 1 \tag{4.38}$$

$$S_{13,\text{ total}} = \frac{1}{\Delta}\sum_{n=1}^{6} P_{n,13}\Delta_{n,13} \tag{4.39}$$

Equation (4.39) calculates the final total S_{13} of the 4-port by using the calculated loops and path gains in (4.3) to (4.8), and (4.25) to (4.38).

4.2.3 S_{31} Total

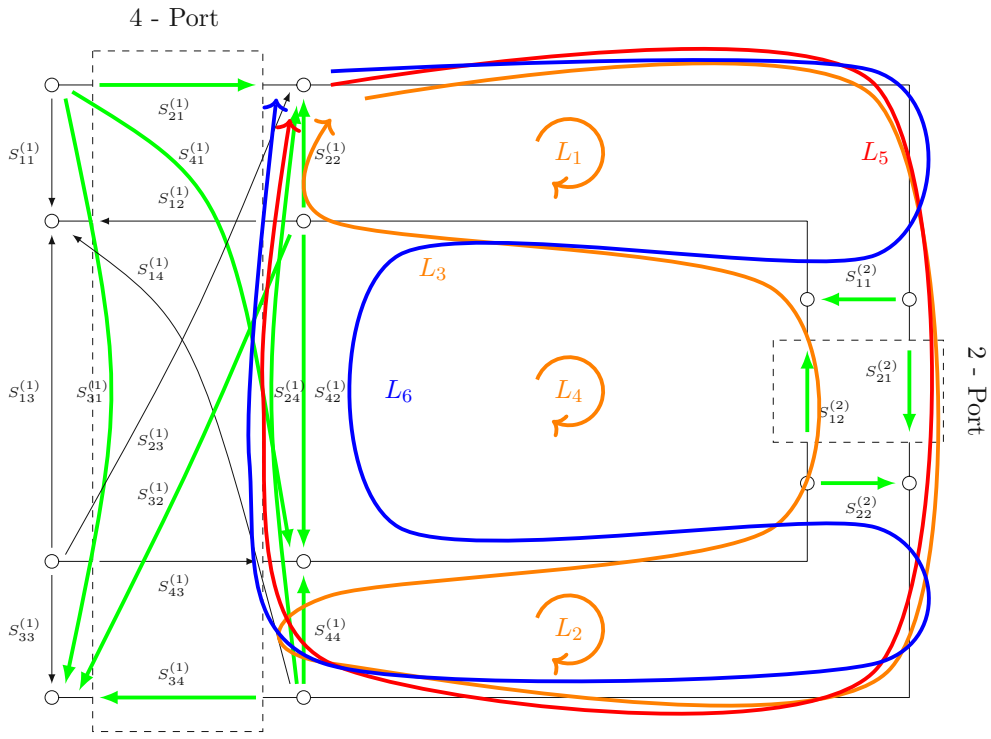

Figure 4.5: Setup constellation for the characterization process of S_{31} total

The total S_{31} is solved exactly with the same techniques as the previous part for S_{11} and S_{13}. The loops and the participating S-Parameters in this calculation are marked in color in Fig. 4.5.

$$P_{1,31} = S_{31}^{(1)} \tag{4.40}$$
$$P_{2,31} = S_{21}^{(1)} S_{11}^{(2)} S_{32}^{(1)} \tag{4.41}$$
$$P_{3,31} = S_{21}^{(1)} S_{21}^{(2)} S_{34}^{(1)} \tag{4.42}$$
$$P_{4,31} = S_{21}^{(1)} S_{21}^{(2)} S_{44}^{(1)} S_{12}^{(2)} S_{32}^{(1)} \tag{4.43}$$
$$P_{5,31} = S_{41}^{(1)} S_{12}^{(2)} S_{32}^{(1)} \tag{4.44}$$
$$P_{6,31} = S_{41}^{(1)} S_{22}^{(2)} S_{34}^{(1)} \tag{4.45}$$
$$P_{7,31} = S_{41}^{(1)} S_{12}^{(2)} S_{22}^{(1)} S_{12}^{(2)} S_{34}^{(1)} \tag{4.46}$$

$$\Delta_{1,31} = 1 - (G_{L_1} + G_{L_2} + G_{L_3} + G_{L_4} + G_{L_5}) + G_{L_1} G_{L_2} \tag{4.47}$$
$$\Delta_{2,31} = 1 - G_{L_2} \tag{4.48}$$
$$\Delta_{3,31} = 1 - G_{L_4} \tag{4.49}$$
$$\Delta_{4,31} = 1 \tag{4.50}$$
$$\Delta_{5,31} = 1 - G_{L_5} \tag{4.51}$$
$$\Delta_{6,31} = 1 - G_{L_1} \tag{4.52}$$
$$\Delta_{7,31} = 1 \tag{4.53}$$

$$S_{31,\text{ total}} = \frac{1}{\Delta} \sum_{n=1}^{6} P_{n,31} \Delta_{n,31} \tag{4.54}$$

Equation (4.54) calculates the final total S_{31} of the 4-port by using the calculated loops and path gains in (4.3)–(4.8), and (4.40) to (4.53).

4.2.4 S_{33} Total

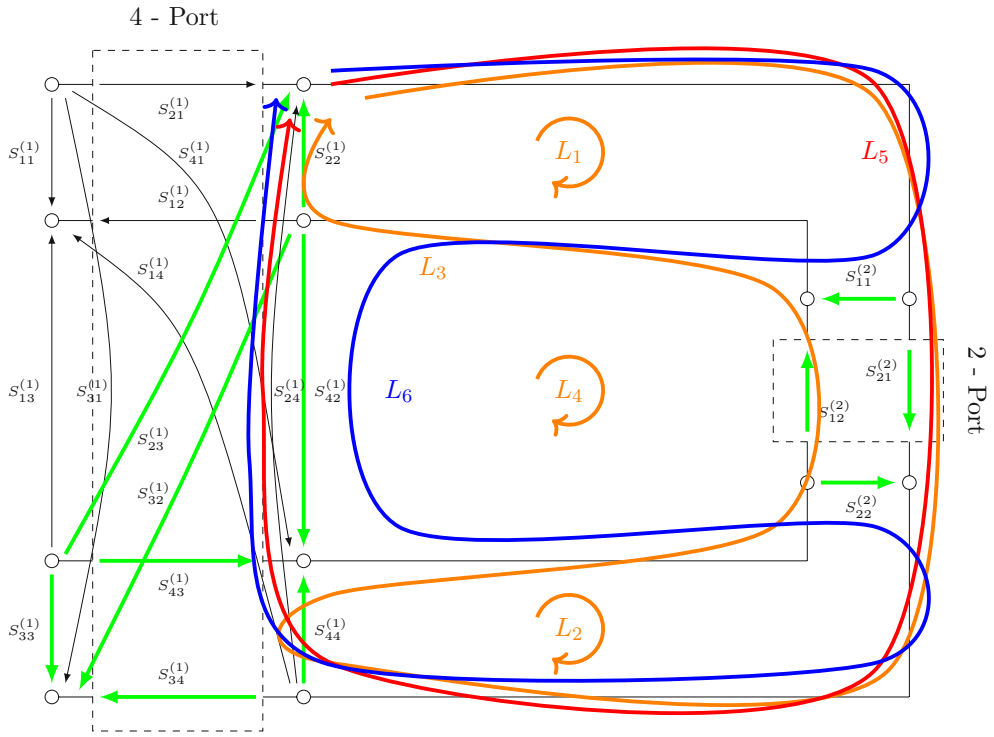

Figure 4.6: Setup constellation for the characterization process of S_{33} total

The total S_{33} is solved exactly with the same techniques as the previous parts for S_{11}, S_{13}, and S_{31}. The loops and the participating S-Parameters in this calculation are marked in color in Fig. 4.6.

$$P_{1,33} = S_{33}^{(1)} \tag{4.55}$$
$$P_{2,33} = S_{43}^{(1)} S_{22}^{(2)} S_{34}^{(1)} \tag{4.56}$$
$$P_{3,33} = S_{43}^{(1)} S_{12}^{(2)} S_{22}^{(1)} S_{21}^{(2)} S_{34}^{(1)} \tag{4.57}$$
$$P_{4,33} = S_{23}^{(1)} S_{11}^{(2)} S_{32}^{(1)} \tag{4.58}$$
$$P_{5,33} = S_{23}^{(1)} S_{21}^{(2)} S_{34}^{(1)} \tag{4.59}$$
$$P_{6,33} = S_{23}^{(1)} S_{11}^{(2)} S_{42}^{(1)} S_{22}^{(2)} S_{34}^{(1)} \tag{4.60}$$
$$P_{7,33} = S_{43}^{(1)} S_{12}^{(2)} S_{32}^{(1)} \tag{4.61}$$

$$\Delta_{1,33} = 1 - (G_{L_1} + G_{L_2} + G_{L_3} + G_{L_4} + G_{L_5}) + G_{L_1} G_{L_2} \tag{4.62}$$
$$\Delta_{2,33} = 1 - G_{L_1} \tag{4.63}$$
$$\Delta_{3,33} = 1 \tag{4.64}$$
$$\Delta_{4,33} = 1 - G_{L_2} \tag{4.65}$$
$$\Delta_{5,33} = 1 - G_{L_4} \tag{4.66}$$
$$\Delta_{6,33} = 1 \tag{4.67}$$
$$\Delta_{7,33} = 1 - G_{L_5} \tag{4.68}$$

$$S_{33,\text{ total}} = \frac{1}{\Delta} \sum_{n=1}^{6} P_{n,33} \Delta_{n,33} \tag{4.69}$$

Equation (4.69) calculates the final total S_{33} of the 4-port by using the calculated loops and path gains in (4.3)–(4.8), and (4.55) to (4.68).

4.2.5 Combination and Validation

For validation of the characterized system, i.e., the combination of S-Parameters of a 4-port and a 2-port, I used the simulation tools of AWR Design Environment. The SModel test compares the calculated S-Parameter file with the simulation of the combination in AWR to check for accuracy and plausibility of my calculations. The AWR SModel test gives perfect results at an error of approximately −110 dB, which is in the range of numerical simulation accuracy.

4.3 Performance Limits on Phase Resolution and Accuracy

Some accuracy indicators for the reader can be infered from phase and RSSI measurements with the characterization setup and the directly connected RFID tag. Measurements with the RFID reader show, that the reported phase and RSSI values are quantized. The reported phase is quantized in steps of $360/64 = 5.625\,°$, and the RSSI in steps of 0.5 dB.

I separated this setup into two independent models to study the behavior of different attenuations and phase shifts of the reverse path from the tag. Measurements showed that RFID tags could be read at an absolute minimum RSSI value of −89 dBm. The standard deviation of the phase reports depends on the received power level. More specifically, the standard deviation of the phase reports for a tag received at −82 dBm is approximately

1.5 times higher than the standard deviation for a tag received at −76 dBm. The corresponding values of the standard deviation for the phase at an RSSI of −82 dBm was $\sigma = 11.3\,°$, and $\sigma = 7.3\,°$ at an RSSI of −76 dBm.

Further investigation of the phase showed an unexpected behavior of the reader's reported phase values. Looking at Fig. 4.7, one can see at the abscissa the phase shift φ_{PS} with the phase shifter in the measurement setup and at the ordinate the phase of the RFID reader φ' (reported) and φ (true). The reported phase values matched well with the expected ones with a gradient of 4, which should be a factor of 2 in theory. The user manual for the RRU4500 RFID reader states that for a full rotation of 360 °, the RFID tag travels a distance of 17 cm, corresponding to a displacement of $\lambda/2$. Since the user manual did not help in solving this issue, Kathrein's customer support was contacted. Their support team [18] confirmed the error in the manual and referred to a technical limitation in the receiver's processor, which reports values in the range from 0 ° to 180 ° only. Their reader's firmware multiplies the measured values from the receivers processor by factor 2 to display the full 360 ° span. A proposed adhoc procedure to empirically correct this reporting error by the RFID reader would be to double the effective operating frequency or to divide the reported phase values by factor 2. This multiplicative factor explains the wrong gradient of the phase for Fig. 4.7.

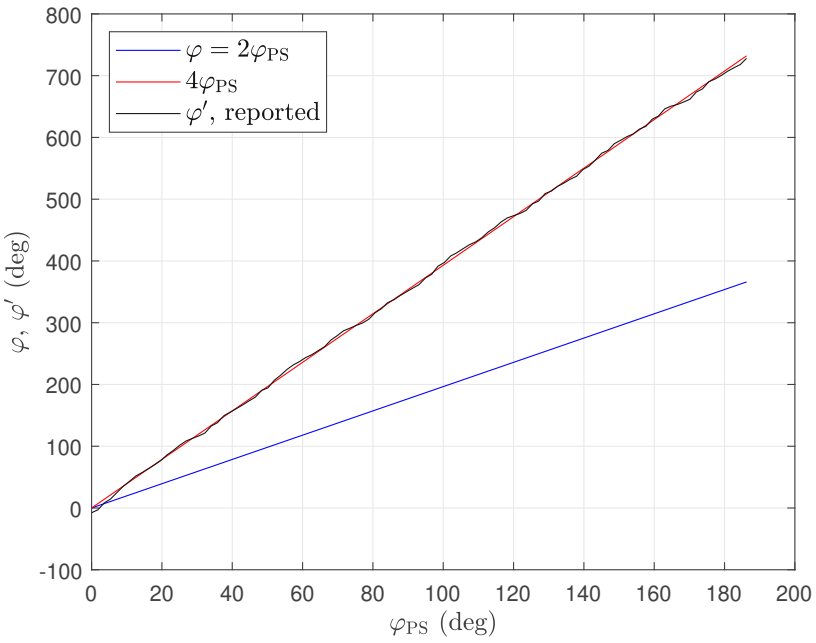

Figure 4.7: Unwrapped phase values from the RFID reader φ (true), φ' (reported) over the phase shifters φ_{PS}

Further details on the behavior of the reported phase values can be seen in the following figures. Fig. 4.8 shows the reported phase values' deviation from the expected ones. The abscissa shows the position φ_{PS} of the phase shifter in the measurement setup and the deviation of the reported phase values from the expected ones at the ordinate. Additionally, Fig. 4.9 shows the standard deviation of the reported phase values over the position of the

phase shifter. Since the reader has a reported phase resolution of approx. 5.6 °, the corresponding deviations from the expected trace with a maximum of 10 °, and the standard deviation with a maximum value of 6.5 ° are not critical for the further development of localization algorithms. Clarifying the unexpected phase behavior of the reported phase values from the RFID reader was also essential.

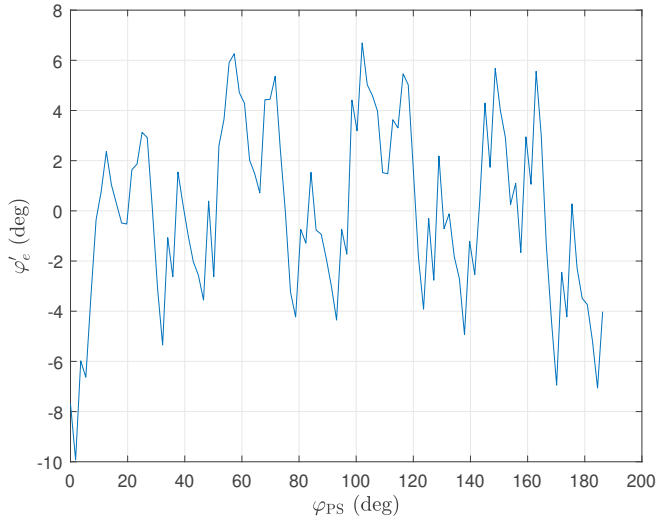

Figure 4.8: Deviation of the reported phase values from the RFID reader over the moved phase from the phase shifter φ_{PS}

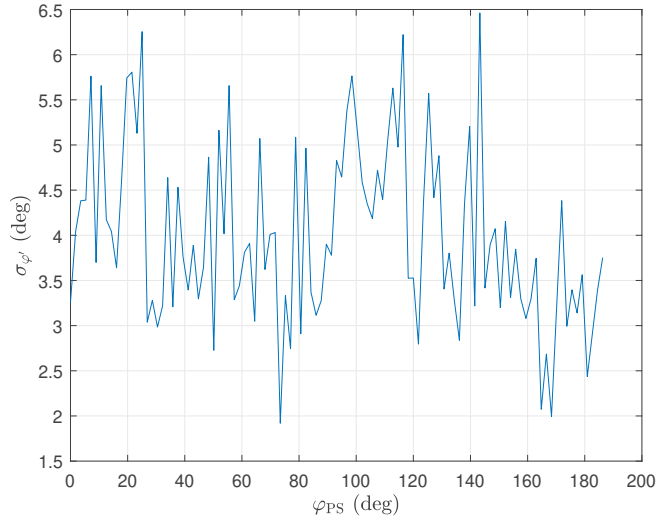

Figure 4.9: Standard deviation $\sigma_{\varphi'}$ of the reported phase values from the RFID reader over the phase shifter φ_{PS}

Considering the error on the reported phase for the phase resolution, one can obtain quantized steps of 2.8 °, providing a resolution of approximately 1.5 mm in distance measurement at a carrier frequency of approximately 868 MHz.

One should also note the influence of temperature variations on phase measurements. As Fig. 4.10a shows, the RFID reader's core temperature rises when transmitting. After continuously running inventory rounds for approximately 30 min, the temperature will settle at a constant value. Supposing these first data in the warmup timespan are not necessarily needed, one could drop these parameters to eliminate the temperature influence on the phase data in a much larger measurement. Fig. 4.10b shows one phase trace from a static RFID tag, where the influence of the temperature change is seen clearly.

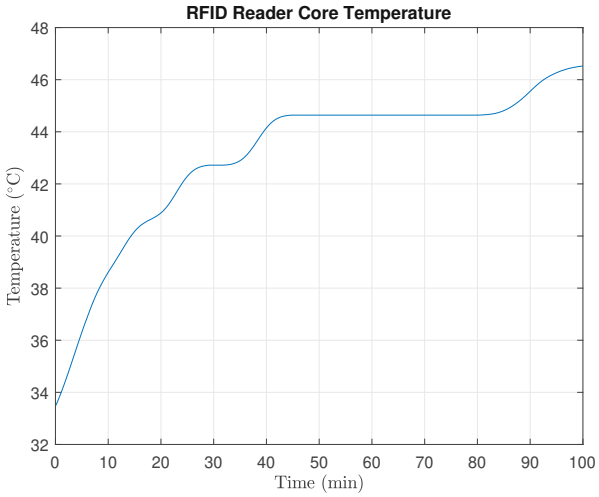

(a)

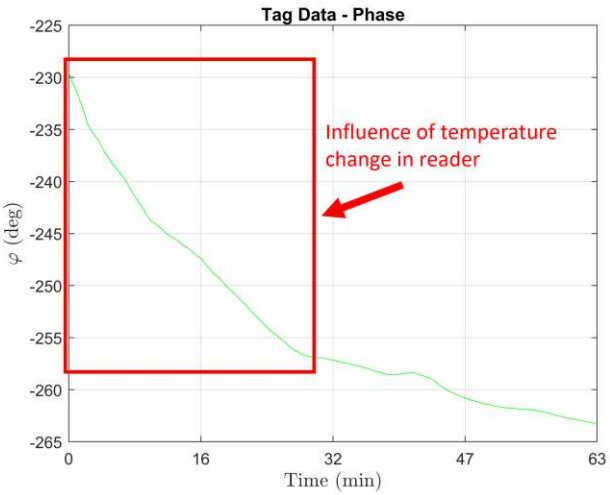

(b)

Figure 4.10: a) RFID reader's core temperature change during measurement; b) Influence of temperature to phase

4.4 Measurement of the Room and Antenna Orientations

For experimental studies it is required to know the true room dimensions, the antenna positions, and their orientation. For these room measurements, it is essential to know the relative position of the antennas to the tags. Therefore, I built a laser measurement unit mounted on two motorized rotating joints to be able to scan the azimuth and elevation. A "PowerCube" from "amtec robotics GmbH" [19] was used for the motorized rotating joints. A gateway was added to enable control via Matlab, converting the serial commands from Matlab via USB to Controller-Area-Network (CAN)-Bus commands for the PowerCube. This gateway consists of an Arduino Uno with a CAN-Bus shield from DFROBOT. The gateway is also equipped with a joystick to enable manual laser measurements. The laser distance measurement unit is controllable via serial connection and communicates with the Matlab script. Fig. 4.11 shows the PowerCube with the laser measurement unit. The gray enclosure of the laser unit is designed to precisely align the laser in all axes. The related model is shown in Fig. 4.12. A detailed instruction on the operation of the measurement unit is given in Appendix E.

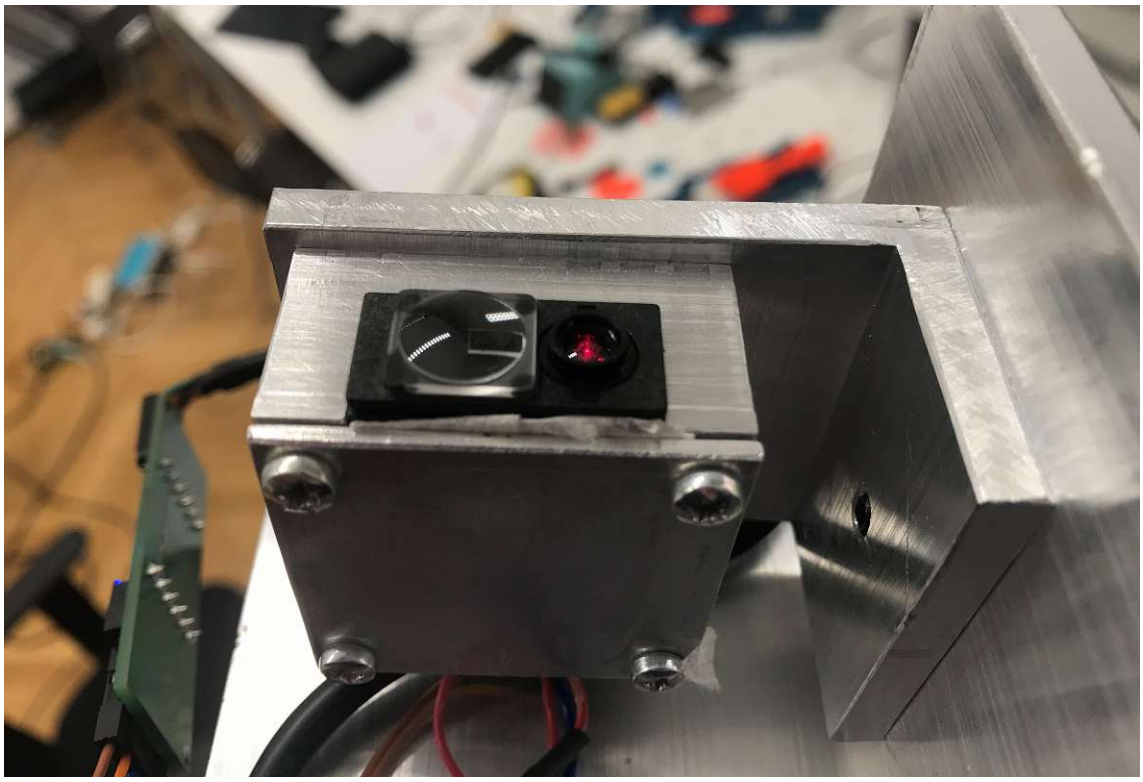

Figure 4.11: Positioning unit with PowerCube and laser distance unit

For the experimental characterization of localization algorithms, it is essential to know the true trajectory of tag movement. Therefore, I built a tag positioner consisting of two PC-controlled, motorized linear axes. The two linear axes cover an area of $0.8\,\mathrm{m} \times 1.49\,\mathrm{m}$. Fig. 4.13 shows the two linear axes. They are controlled via a CAN-to-USB adapter and a corresponding Matlab script.

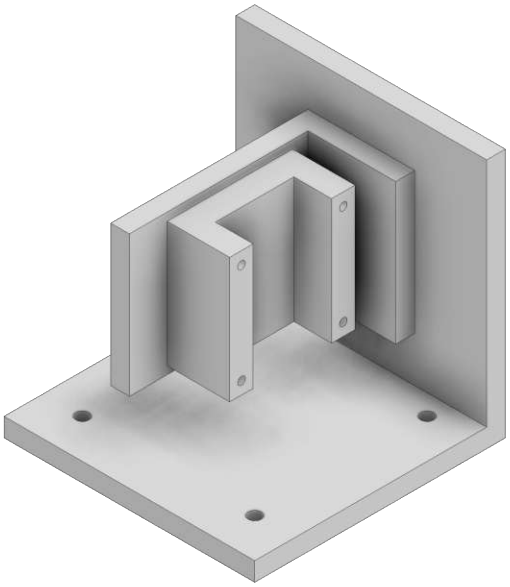

Figure 4.12: 3D model for laser alignment on the PowerCube

Figure 4.13: Tag positioner for precisely moving a tag during the measurements

5 Measurement Campaign

A measurement campaign was carried out to investigate the performance of the measurement platform, acquire RFID data for various environmental conditions, acquire information on the readability of tags in different areas, and further validation. The first measurement in this chapter covers readability analysis for a defined area in the center of the room. This measurement's purpose was to find the overall coverage from the wide-range antennas. The second part of this measurement campaign was to gain more data about readability in positions close to objects in different spaces, including the room's edges. The third part of this campaign covers analysis and statistical analysis of AoA applications to linear movements of the tags. The campaign took place at the "Institute of Electrodynamics, Microwave and Circuit Engineering (EMCE)" at TU Wien in room No. CF0135. This room has dimensions of $6\,\mathrm{m} \times 5.2\,\mathrm{m} \times 4\,\mathrm{m}$ (length, width, height).

The overall setup for the measurements consists of the same configuration as seen in the introduction of the platform in Fig. 3.1. Position information and the corresponding numbering of the antennas can be found in Tab. 5.1 and Fig. 5.1. The large wide-range antennas were placed in the top four corners, and the mid-range antennas were placed above some workplaces. Measurement of the antenna positions and their orientations was done with the constructed laser distance measurement unit from Fig. 4.11. The green rectangle in Fig. 5.1 shows the area used for this campaign's first measurement. Transmission of inventory rounds and decoding of the received data sets in all measurements is done with Matlab. A detailed description of the data collection with the Matlab interface is shown in Section 3.5.

Compared to the second and third part of this chapter, the antenna configuration slightly deviates for the first measurement. All wide-range antennas in the top corners were selected, but only the first two MIRA-100 antennas (antennas 3 and 4) were placed vertically on a tripod pointing to the desired area where the linear axes were located. Since the other mid-range antennas were not likely to obtain useful data for this area, they were excluded, saving valuable airtime.

Antenna No.	Main	Sub	Antenna Type	Name
1	1	1	WRA7070	W1/1
2	1	2	WRA7070	W1/2
3	1	3	MIRA-100	M1/1
4	1	4	MIRA-100	M1/2
5	2	1	WRA7070	W2/1
6	2	2	WRA7070	W2/2
7	2	3	MIRA-100	M2/1
8	2	4	MIRA-100	M2/2
9	3	1	WRA7070	W3/1
10	3	2	WRA7070	W3/2
11	3	3	MIRA-100	M3/1
12	3	4	WRA7070	W3/3
13	4	1	WRA7070	W4/1
14	4	2	WRA7070	W4/2
15	4	3	MIRA-100	M4/1
16	4	4	Reference Tag	

Table 5.1: Mapping of antennas and reference tag to reader main and sub port

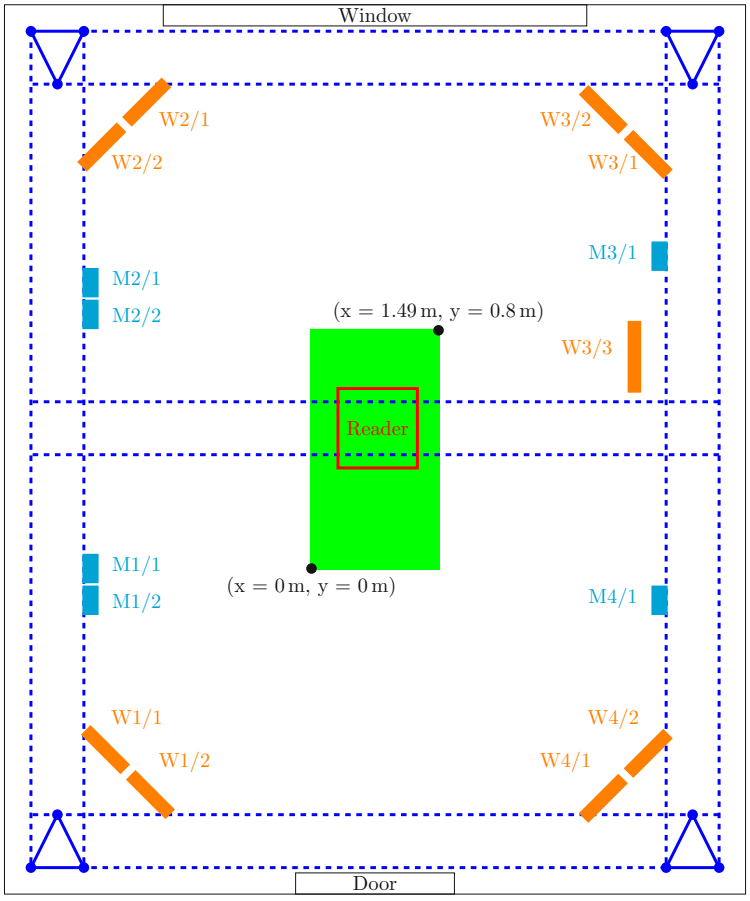

Figure 5.1: Antenna mapping in the measurement room No. CF0135

5.1 Readability and Phase Measurement in a Limited Area

Starting the measurements with an area that is covered by the PowerCube tag positioner with dimensions 1.49 m × 0.8 m in a spacing interval of 1 cm, the purpose was to learn about readability, RSSI range, and the phase behavior of RFID tags in that grid. Fig. 5.2 shows the area the tag traveled and the antenna points marked with relevant coordinate information. Referring to the antenna mapping in Tab. 5.1, antennas 1–6, 9, 10, and 12–14 were selected for the subsequent measurements.

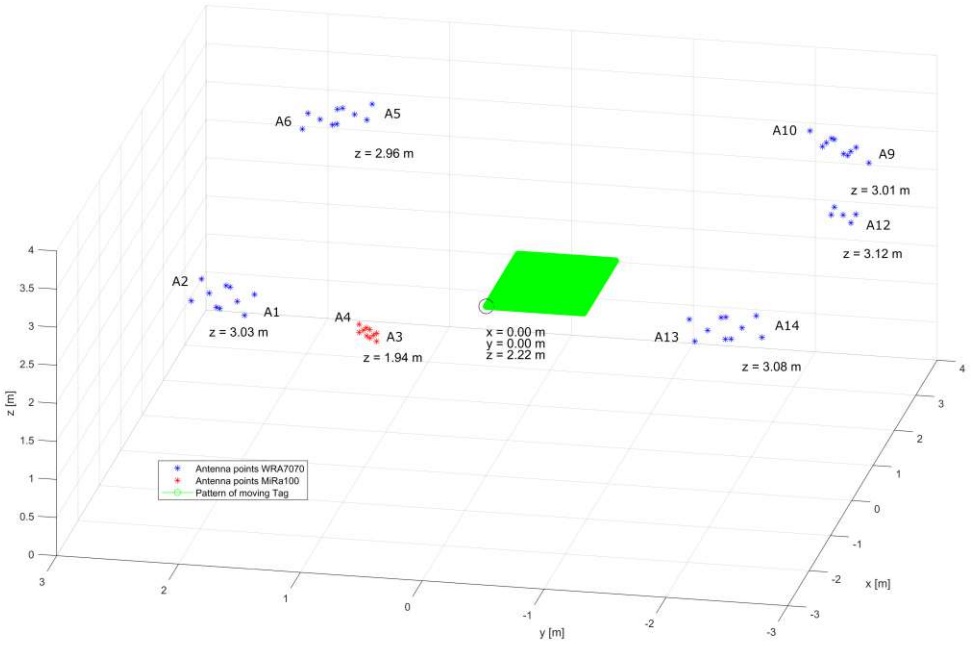

Figure 5.2: Antenna positions and traveled area

For the first run, a single RFID tag is placed in horizontally polarized orientation on the top of two poles (Fig. 5.3 left), extending the tag positioner in its height to avoid reflections from the ground structure. The measurement process was set up to process 10 inventory runs at each antenna and at each interval point. These maximum ten result values were later averaged in the subsequent data processing.
Figs. 5.4a and 5.4b show the phase and RSSI pattern for antenna 1. From the origin in these figures, the antenna is approximately at 2.5 m distance to the bottom right on the traverse construction. The white areas in both figures represent the fields where the RFID tag could not be read a single time.

In the investigation of the phase pattern in Fig. 5.4a and at a more detailed form in Fig. 5.5, one can see that the reader turns the phase values from 0 ° to 360 ° in a travel distance of $\lambda/4$ for an RFID tag, which is obviously wrong to theory. As discussed in Section 4.3, and confirmed by Kathrein's support team [18], this phase error is due to technical limitations of the receiver's processor in the RFID reader.

One can see patterns for antenna 1 in Figs. 5.4 and 5.5 that match the position of the antenna, but with many areas with missing data where the tag could not be read. Therefore,

Figure 5.3: Horizontal RFID tag mount (left), vertical RFID tag mount (right)

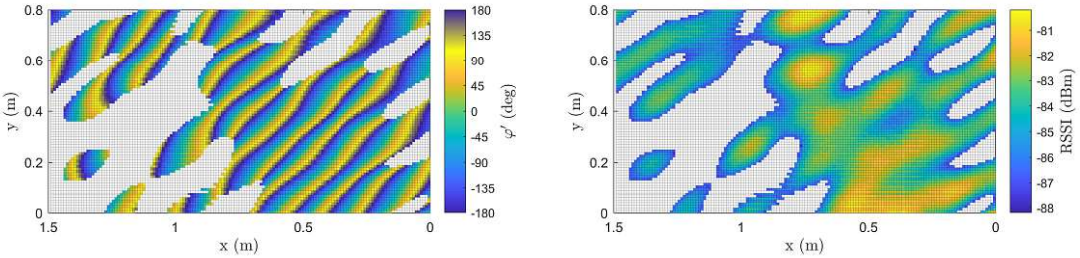

(a) **(b)**

Figure 5.4: a) Reported phase and b) RSSI pattern for antenna 1; horizontal tag mount

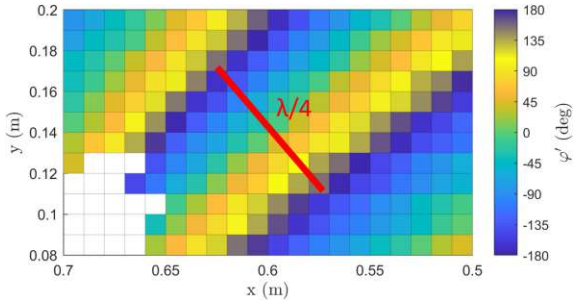

Figure 5.5: Detailed view for the reported phase pattern from antenna 1; horizontal tag mount

the RFID tag was mounted in vertical polarized orientation on the top of the two poles for the following measurements. The change in orientation is shown in Fig. 5.3. The two black poles extend the positioner with the two PowerCube axes up to 2 m in height. On the top of the poles is the RFID tag mounted to a piece of Rohacell 31 HF. This material is made from Polymethacrylimide (PMI), was invented by Evonik Industries, and features good mechanical and electrical properties with a relative permittivity $\epsilon_r \approx 1.04$ [20].

Comparing Figs. 5.4 and 5.6, a clear difference in readability is observed due to the changed

tag's orientation. Especially at lower incidence angles, the tag appears smaller for the antenna at and may not be read as frequently as for vertical polarized tags. Figs. 5.6a and 5.6b have significantly fewer empty areas than the measurement with the horizontally mounted tag. Looking at the upper left quarter in Fig. 5.6, one can see a mixture in the phase pattern. This occurs due to multipath propagation, i.e., the ratio of the field strength for the direct path and a second path may become one.

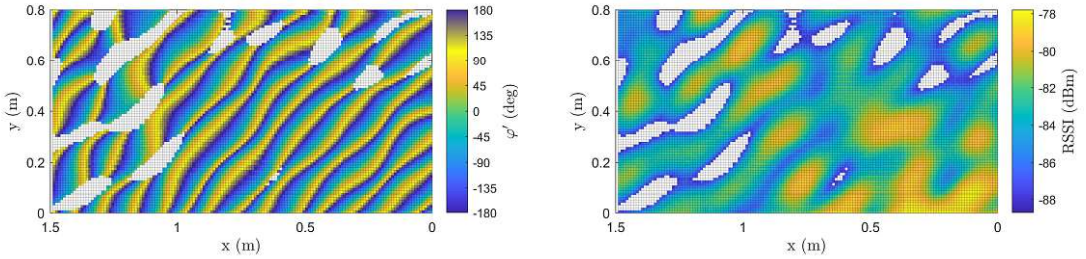

(a) **(b)**

Figure 5.6: a) Reported phase and b) RSSI pattern for antenna 1; vertical tag mount

Figs. 5.7 and 5.8 show the phase and RSSI patterns for the two MIRA-100 antennas placed close to the side (y=0) of the positioner. The exact position for the mid-range MIRA-100 antennas can be obtained from the red points in Fig. 5.2. These patterns clearly show that also the mid-range antennas work well in their near-field, but are significantly affected by their smaller gain and cable, which is 4 m longer compared to the wide-range antennas.

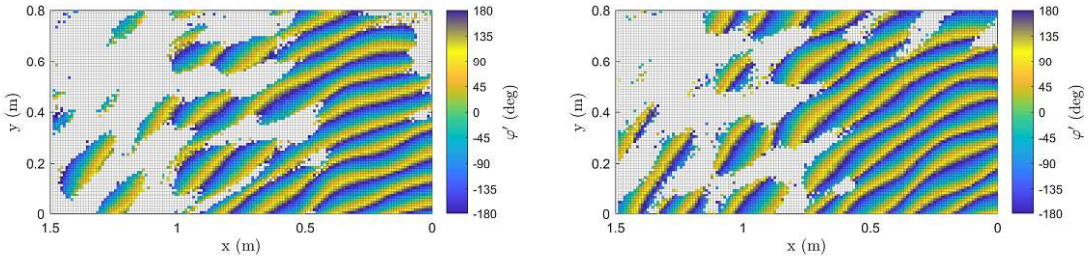

(a) **(b)**

Figure 5.7: Reported phase pattern for a) antenna 3 and b) antenna 4; vertical mounted tag

Fig. 5.9 shows the illustration of the standard deviation for antenna 1 with the vertically polarized RFID tag. One can see from this figure an overall stable phase behavior, which is promising for further development of localization algorithms. If the standard deviation in the phase values showed strong fluctuations, the RFID reader would be useless for our system. The standard deviation was calculated with the corresponding Matlab function "std" over the dimension for the number of reads. This function calculates the standard deviation with (5.1) for the reported phase vector $\underline{\varphi'}$ with length N and its mean μ.

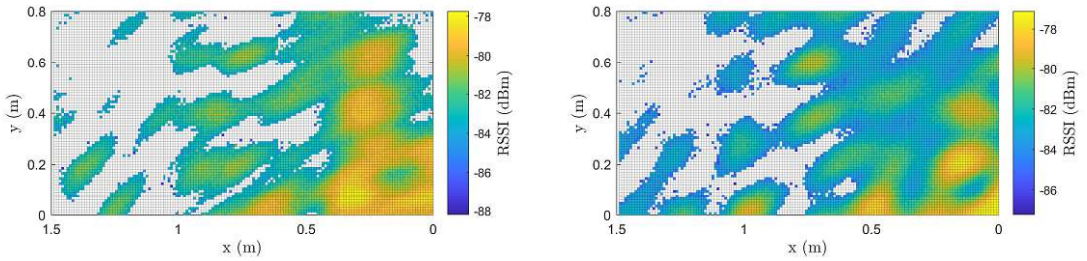

(a) **(b)**

Figure 5.8: RSSI pattern for a) antenna 3 and b) antenna 4; vertical mounted tag

$$\sigma_{\varphi'} = \sqrt{\frac{1}{N-1}\sum_{i=1}^{N}|\varphi'_i - \mu|^2} \tag{5.1}$$

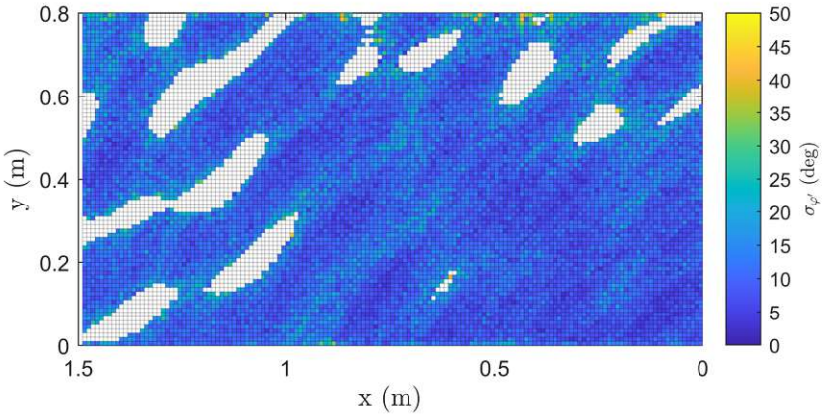

Figure 5.9: Standard deviation $\sigma_{\varphi'}$ for the reported phase on antenna 1; vertical mounted tag

Looking at Fig. 5.10, one can clearly see that in most cases, all ten reads could be done successfully. Only for the results at the edges to the empty fields, widely varying numbers of reads occur. Some orange fields also exist in areas of the figure where low RSSI values appeared. They are still at a read percentage of approximately 80 % for this test, which shows that the reader can still read the tag consistently under poor conditions.

The remaining selected antennas provide similar results as it can be seen for antennas 1 and 2. Concluding these measurements, the system could read the tag from all antennas with overall few missing areas at a holistic view. Still, some empty regions exist where the reader could not read the tag due to destructive interference. If the results from

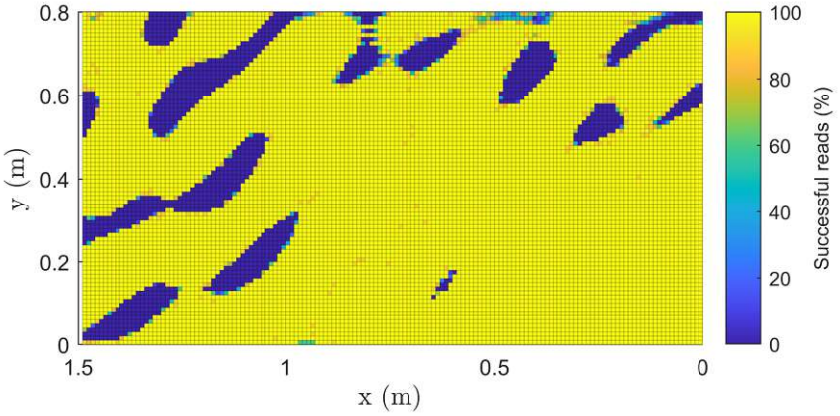

Figure 5.10: Map of successful read counts for 10 trials at each position on antenna 1; vertical mounted tag

all antennas are considered, there is no longer an empty field in a holistic view. Since this measurement covered only a small area compared to the total room size, the next measurement deals with finding the coverage of stationary RFID tags at places on outer edges of the room, including workplaces.

5.2 Measurement for Stationary Tags

This measurement was done to gain knowledge of the overall readability of RFID tags distributed in the outer edges of the room and their phase and RSSI behavior on all antennas for extended periods. For this purpose, six RFID tags were placed in different locations in the room, the measurement timespan was set to 2 h, and all 16 antennas were used. The actual tag positions can be seen in Fig. 5.11. Since the previous measurement covered analysis of an area in the center of the room, this measurement's strategy was to look at the antennas' coverages in outer locations in the room. The tag with number 1 is the reference tag, which was directly connected to a switch port to obtain phase data which is not influenced by dynamic movements in the room. A phase reference in the system is also profitable to counteract phase influences from reader internal temperature changes, as it is shown in Fig. 4.10. Tag 2 was placed directly on a workplace and below a mid-range antenna. Tag 3 was set on a wooden shelf to check the coverage from wide-range antennas across the room. This scenario is important in case a tag may be out of the range of a mid-range antenna. Tags 4 and 6 were placed for the same purpose as tag 3 but located close to different objects. Tag 4 was placed next to the computer and tag 6 on a slightly elevated position on a carton box. Corresponding to the previous measurement, tag 5 was positioned in the center of the room to check the coverage of the wide-range antennas for longer measurement periods.

Right after the measurement finished, all data sets of the different RFID tags detected in the room were extracted. The constellations of Fig. 5.12a to Fig. 5.12f show the distribu-

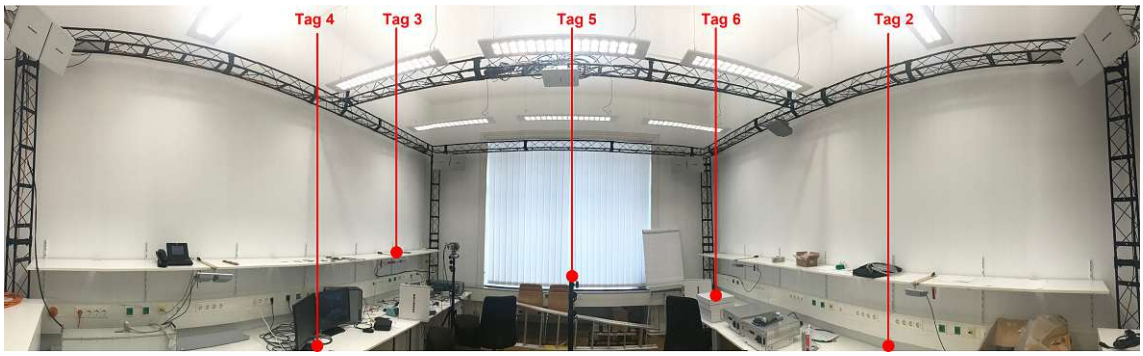

Figure 5.11: Distribution of RFID tags in the room for static measurements

tions of the number of reads for the six sample tags in the room to the 15 antennas.

Fig. 5.12a is the distribution of the reference tag, which is just detected on the last antenna port since it is connected directly to the switch on the fourth main antenna port and the fourth sub port. There is nothing special about the reference tag since it constantly answers equally on all four used frequency channels. This is used for test purposes to have a reference phase in the system to be able to remove dynamic temperature changes influencing the phase values.
The port distribution in Fig. 5.12b shows the sample tag with number 2, picked up by all antennas at the main port 4, except the port with the reference tag. Again, this tag can be read uniformly on all four channels. Since it was not detected by the remaining antennas, it was simply assumed to be too far away from them. The corresponding actual position can be seen in Fig. 5.11.
Analyzing the port distribution on the third RFID tag in Fig. 5.12c, one can see that it was read mainly by antennas 5 and 6, much less by antenna 13, and just barely by antennas 7 and 8. This is due to the RFID tag sitting behind the two MIRA-100 antennas on a piece of a wooden shelf.
The port distribution of the fourth RFID tag in Fig. 5.12d shows an interesting behavior. This tag sits in between the two workplaces to antennas 1 to 8 on the left side in the room, but is slightly more placed to antennas 1 to 4 on the table as seen in the photo in Fig. 5.11. This tag with identification number 4 can be read clearly by the first two large WRA7070 antennas and the first two small MIRA-100 antennas. Also, antenna 13 had good read capabilities to this tag's position. The results on antennas 5 and 10 show perfectly that it is essential to use different frequencies since they could not read this RFID tag at the first channel (865.7 MHz).
The port distribution of Fig. 5.12e shows the RFID tag sitting on a pole in the center of the room. This can also be seen on the antennas that picked this tag up. Since this RFID tag is far away from the MIRA-100 antennas, it had only been read by the larger WRA antennas. Again, it shows close to uniformly read numbers at all four frequencies. The actual tag's position is also shown in the center of Fig. 5.11.
The last port distribution in Fig. 5.12f shows an RFID tag sitting on a small box at a table close to a MIRA-100 antenna (no. 11). This tag is mainly read by the nearest antenna 11 and other WRA7070 antennas (W1/2, W2/1, W2/2, W3/1, W3/3).

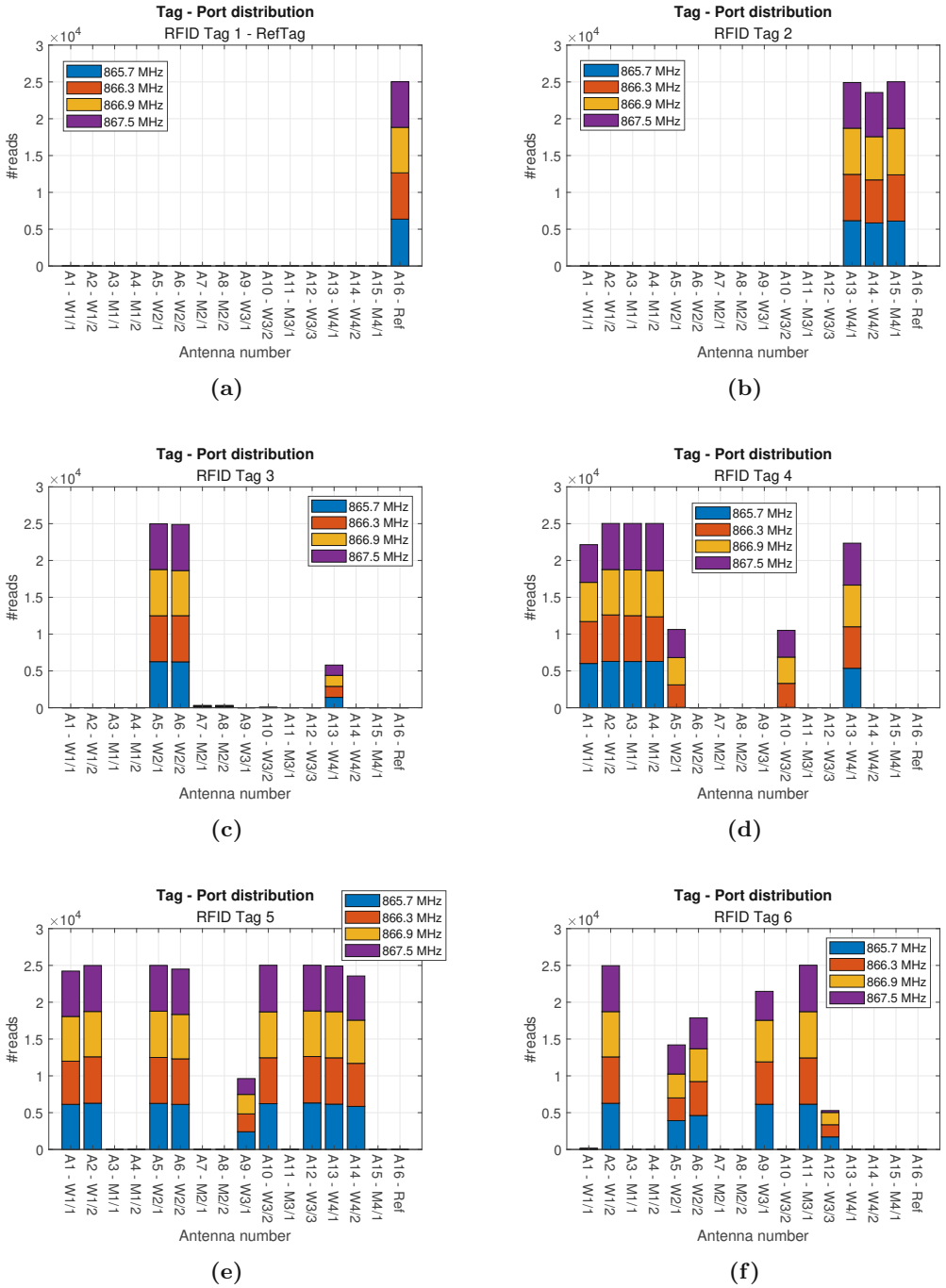

Figure 5.12: Distribution of successful reads over antenna and channel

When extracting the phase trace of an antenna for the tag in the center of the room, one can see an overall stationary phase in Fig. 5.13, but with a small dent around $t = 81$ min, related to a person walking in the room. This phase behavior shows the obstruction of the LOS path, where reflected and NLOS paths are stronger at the reader and therefore deliver different phase values. Additionally, one can see in Fig. 5.13 again the phase drift due to temperature changes in the first 30 min, as seen in Fig. 4.10.

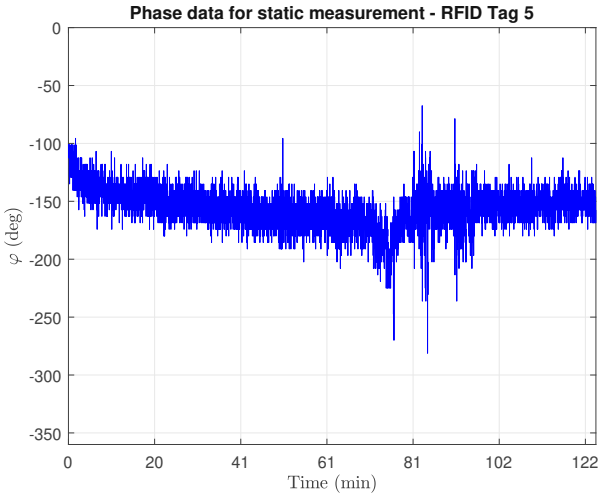

Figure 5.13: Tag phase for measurement of 2 h from antenna 6

Concluding this static measurement, one can get an idea of the different areas and where each antenna is capable of reading tags. In Fig. 5.12d, antennas 5 and 10 show good examples for the case where a tag could not be read at all frequencies, i.e., there do not exist results for the frequency 865.7 MHz. This behavior indicates that it is essential to use several alternating channels for reasonable read rates. Sometimes it also occurs, that a wide-range antenna picks up a tag and the other wide-range antenna right next to it never reads this tag, which happens mostly at edge areas. In general, all distributed tags could be read and the system also delivers constant phase values over longer measurement periods. This measurement performed over 600 000 reads in total.

5.3 Angle of Arrival Analysis

The preceding two measurements have given good results and important findings on the overall coverage of the antennas and the behavior of the reader's provided data. Moving one step toward localization algorithms, further attempts like AoA tests can now be made with this system. The first scenario is a linear movement with consistent LOS, and the second scenario is a brief statistical analysis of AoA repeatability.

The linear movement of an RFID tag was done in front of a pair of MIRA-100 antennas. Fig. 5.14 shows the antenna and tag setup. The linear movement was done with the constructed tag positioner.

Figure 5.14: AoA LOS scenario

To allow for accurate AoA measurements, I needed calibration data for both MIRA-100 antennas first. For calibration, an RFID tag was placed to a defined position on the front surface of an antenna and a couple of inventory rounds were performed. This procedure was repeated also for the second MIRA-100 antenna. After all preparations were done, I started the measurement process and the movement with the linear axis. Fig. 5.15a shows the phase traces for each antenna. Additionally, Fig. 5.15b shows the corresponding RSSI trace for antennas 3 and 4. One can clearly see that the entropy of the phase traces is much higher than for the RSSI traces. Thus, the RSSI values will be less important in developing further localization algorithms.

One needs to consider in the calculation of the Angle of Arrival that the RFID reader provides wrong phase data, which needs to be compensated by taking the reported phase values φ' times 1/2. Equation (5.2) for the reported phase difference consists of the

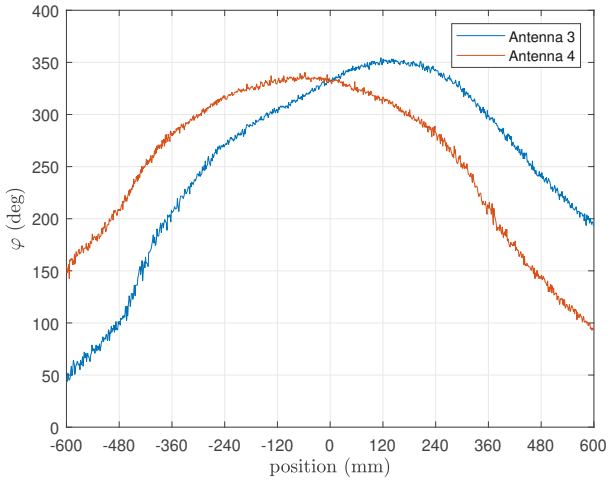

(a)

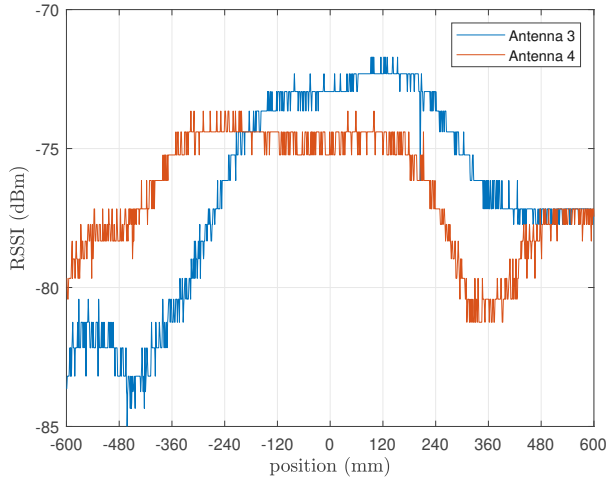

(b)

Figure 5.15: Angle of Arrival LOS scenario: a) true phase traces for antenna 3 and 4; b) RSSI traces for antennas 3 and 4

wavelength λ, the frequency f, and the path difference Δd. Finally, using the true phase φ from the reported phase φ' and the geometric relation for the path difference $\Delta d = d_{\text{ant}} \sin\theta$, the corresponding angle θ can be calculated by (5.3).

$$\Delta\varphi' = 2\pi\frac{\Delta d}{\lambda} \tag{5.2}$$

$$\theta = \arcsin\left(\frac{\lambda}{2\pi d_{\text{ant}}}\Delta\varphi'\right) = \arcsin\left(\frac{\lambda}{\pi d_{\text{ant}}}\Delta\varphi\right) \tag{5.3}$$

Fig. 5.16 shows the estimated and the idealized AoA for this LOS measurement. Fig. 5.17 displays this scenario's error on the calculated AoA. These results are promising, but this is achievable only under perfect LOS conditions with less reflections than at lower heights, which is not a common scenario. All the requirements to get feasible AoA data make this method less viable for further and more complex localization algorithms.

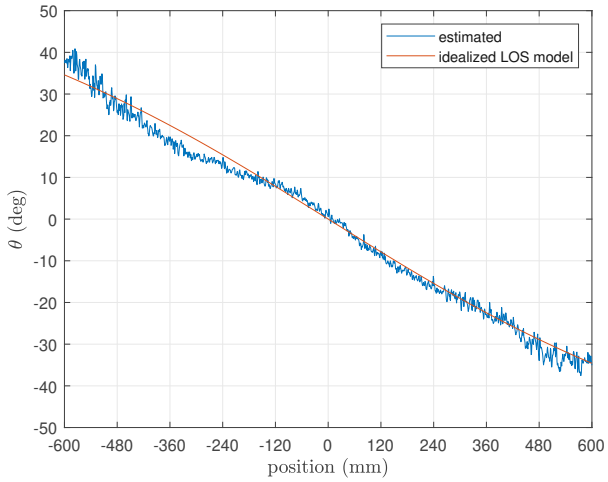

Figure 5.16: Angle of Arrival for the LOS scenario

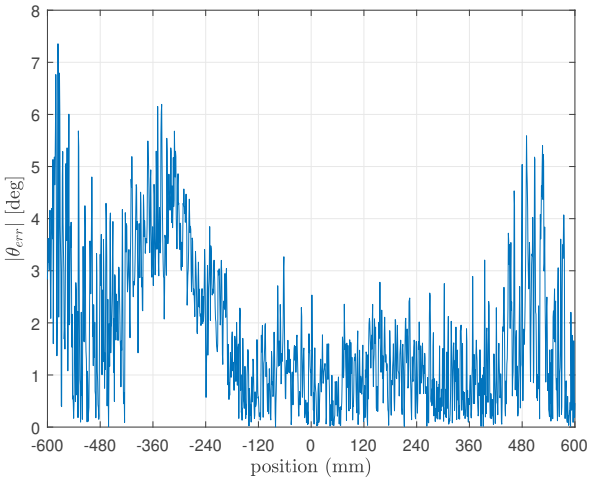

Figure 5.17: Absolute Difference between an idealized LOS model and the calculated Angle of Arrival

To analyze the accuracy and the repeatability of the AoA method, another measurement was performed with slightly different geometric changes for the positions of the antennas and linear axes to the previous AoA measurement. The rest of the setup, including the two mid-range antennas and the Kathrein RFID reader were without changes. Only the linear axis was a bit further away from the antenna pair for these multiple measurements. Two MIRA-100 antennas were set again to a higher position to have fewer reflections from close objects on the ground, e.g., tables, chairs. The distance from the antenna pair to the linear axis was approximately 1 m, and the traveled path for the RFID tag was 1.1 m. Looking at the position at 300 mm in Fig. 5.18, one can see a deviation of max. 15 °. This deviation leads to an uncertainty error of approx. 15–30 cm in this experiment.

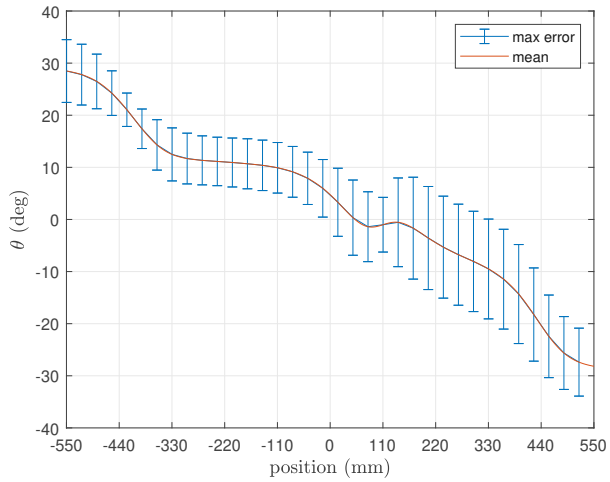

Figure 5.18: Statistical analysis for multiple AoA measurements

The results in Fig. 5.18 show that this method gives an estimate in which range the tag could be but with way too much spreading in range for repeatable and accurate localization algorithms. This inaccuracy is not feasible for the localization of RFID tags, where one needs to be able to see the precise positions of objects and not just to estimate a very vague position of the RFID tag.

6 Conclusions

During my work on this thesis, I have created an experimental platform that enables phase-based UHF RFID measurements from 16 antennas with accurate timing information. This platform aims to enable high-quality and reliable RFID phase measurements, making further research on localization in pharmaceutical rooms possible.

As I wanted to maximize read rates, I studied the communication protocols, analyzed the RFID reader unit and investigated various antenna models. The decision was made against modern reconfigurable antennas, e.g., Kathrein's KRAI antennas, since the exchange of control information would slow down the reading process.

The overall measurement concept employs 16 antennas to obtain nearly complete coverage by antenna diversity in the room. Since the maximum number of antenna ports found in a state-of-the-art commercial reader does not exceed four, the available antenna ports were multiplexed by using four RF switches. These switches are controlled by my self-designed and programmed additional hardware, called the controller, and synchronized with the RFID reader using its GPIO port. The controller communicates with a Matlab user interface, using an XPort Serial-to-Ethernet bridge.

To characterize the RFID reader and its accuracy in phase and RSSI values, I did measurements using a setup composed of a variable RF step attenuator, a phase shifter, and a directly connected RFID tag. These measurements showed an unexpected behavior of the reader's reported phase, clarified by Kathrein's customer support. The resulting resolution and standard deviation of the phase do not indicate issues for further research projects.

For upcoming development of localization algorithms and deployment of the corresponding systems, it is essential to know the relative distances between the antennas. Therefore, I created a precise laser ranger with two PowerCube axes. This device provides the operator data on azimuth, elevation, and distance to the measured points, which can be used to create 3D models of the environment.

A measurement campaign was performed to analyze the readability at different room positions, the antenna coverage, and the phase stability. It clearly showed differences in the readability for vertically and horizontally polarized tag orientations. Analysis of the phase stability gave promising results with a small standard deviation, which is a requirement for further research on localization algorithms, e.g., using probabilistic ML [21]. As expected, the antenna analysis showed good room-coverage for the wide-range antennas, while the mid-range antennas are more suitable for workplaces. Further AoA

experiments were done to investigate the accuracy and stability of the results. These show good performance for LOS scenarios but are not suitable for multipath scenarios with many reflections or obstructions.

Concluding the work done in this thesis, one can now use the created experimental platform for obtaining high-quality data sets of multiple stationary and moving RFID tags, including precise timestamps, EPC, antenna port numbers, phase, and RSSI values.

References

[1] Holger Arthaber. Spread-Spectrum based Ranging/Localization of UHF RFID Tags. Microwave and Radio Electronics Week (MAREW) 2021, Brno, Czech Republic, Jul. 21, 2021. 2, 12

[2] ETSI EN 302 208 V3.3.1 (2020-08). `https://www.etsi.org/deliver/etsi_en/302200_302299/302208/03.03.01_60/en_302208v030301p.pdf`, online, last accessed Aug. 20, 2022. 2

[3] EPC Global Standard Specification for RFID Air Interface, Class-1 Gen-2 UHF RFID, Version 1.2. `https://www.gs1.org/sites/default/files/docs/epc/uhfc1g2_1_2_0-standard-20080511.pdf`, online, last accessed May 25, 2022. 3, 15

[4] Chenyang Li, Lingfei Mo, and Dongkai Zhang. Review on UHF RFID Localization Methods. *IEEE Journal of Radio Frequency Identification*, 3(4):205–215, 2019. doi:10.1109/JRFID.2019.2924346. 4, 6, 9

[5] Holger Arthaber. Method and system for locating objects. `https://patents.google.com/patent/EP2739989A1/en`, 2011/2012. EP2739989A1, European Patent Office. 4

[6] Andreas Parr. *Konzeption und Optimierung neuartiger Verfahren für die phasenbasierte UHF-RFID-Lokalisierung mit synthetischen Aperturen.* PhD thesis, Friedrich-Alexander-Universität Erlangen-Nürnberg (FAU), 2022. 4

[7] Salah Azzouzi, Markus Cremer, Uwe Dettmar, Rainer Kronberger, and Thomas Knie. New measurement results for the localization of UHF RFID transponders using an Angle of Arrival (AoA) approach. In *2011 IEEE International Conference on RFID*, pages 91–97, 2011. doi:10.1109/RFID.2011.5764607. 6

[8] Alan Bensky. Chapter 14 - Technologies and Applications. In *Short-range Wireless Communication (Third Edition)*, pages 387–430. Newnes, 2019. ISBN 978-0-12-815405-2. doi:10.1016/B978-0-12-815405-2.00014-2. 6, 7, 8, 10, 11

[9] Rabie Fadil, Badr Abou El Majd, Hassan El Ghazi, and Rahil Hicham. Optimizing the Multi-Objective Deployment Problem of mlat System. *MATEC Web of Conferences*, 200:00014, January 2018. doi:10.1051/matecconf/201820000014. 7, 8

[10] Jeffrey Hightower, Gaetano Borriello, and Roy Want. SpotON: An Indoor 3D Location Sensing Technology Based on RF Signal Strength. Mar. 2000. 10

[11] Chitra R. Karanam, Belal Korany, and Yasamin Mostofi. Magnitude-Based Angle-of-Arrival Estimation, Localization, and Target Tracking. In *2018 17th ACM/IEEE International Conference on Information Processing in Sensor Networks (IPSN)*, pages 254–265, 2018. doi:10.1109/IPSN.2018.00053. 10

[12] Mugahid Omer and Yachao Ran. Indoor localization systems for passive UHF RFID tag based on RSSI radio map database. *Progress In Electromagnetics Research M*, 77:51–60, Jan. 2019. doi:10.2528/PIERM18082904. 10

[13] Stefan Nosović, Alois Ascher, Johannes Lechner, and Bernd Bruegge. 2-D localization of passive UHF RFID tags using location fingerprinting. In *2016 8th International Congress on Ultra Modern Telecommunications and Control Systems and Workshops (ICUMT)*, pages 207–212, 2016. doi:10.1109/ICUMT.2016.7765358. 10, 11

[14] Mugahid Omer and Gui Yun Tian. Indoor distance estimation for passive UHF RFID tag based on RSSI and RCS. *Measurement*, 127:425–430, 2018. ISSN 0263-2241. doi:10.1016/j.measurement.2018.05.116. 11

[15] Shuai Shao and Robert J. Burkholder. Item-Level RFID Tag Location Sensing Utilizing Reader Antenna Spatial Diversity. *IEEE Sensors Journal*, 13(10):3767–3774, 2013. doi:10.1109/JSEN.2013.2272216. 11

[16] Samer S. Saab and Zahi S. Nakad. A Standalone RFID Indoor Positioning System Using Passive Tags. *IEEE Transactions on Industrial Electronics*, 58(5):1961–1970, 2011. doi:10.1109/TIE.2010.2055774. 11

[17] Milwaukee School of Engineering. Mason's Gain Formula. `https://faculty-web.msoe.edu/meier/ee3720/technotes/masons.pdf`, online, last accessed Jun. 1, 2022. 23

[18] Holger Busse. Private communication with Holger Arthaber, Aug. 2022. 31, 38

[19] Amtec Robotics. PowerCube User Manual. `http://technix.in.tu-clausthal.de/site/Projekte/IndRobotArm/doku/Handbuch.pdf`, online, last accessed Aug. 18, 2022. 34

[20] Rohacell 31 HF Polymethacrylimide - Evonik Industries. `https://performance-foams.evonik.com/en/products-and-solutions/rohacell/attachment/140034?rev=794f98c8bd5fde83bf7a48c583636425`, online, last accessed Aug. 22, 2022. 39

[21] Kevin P. Murphy. *Probabilistic Machine Learning: An introduction*. MIT Press, 2022. URL `probml.ai`. 50

Appendices

A Controller Schematic

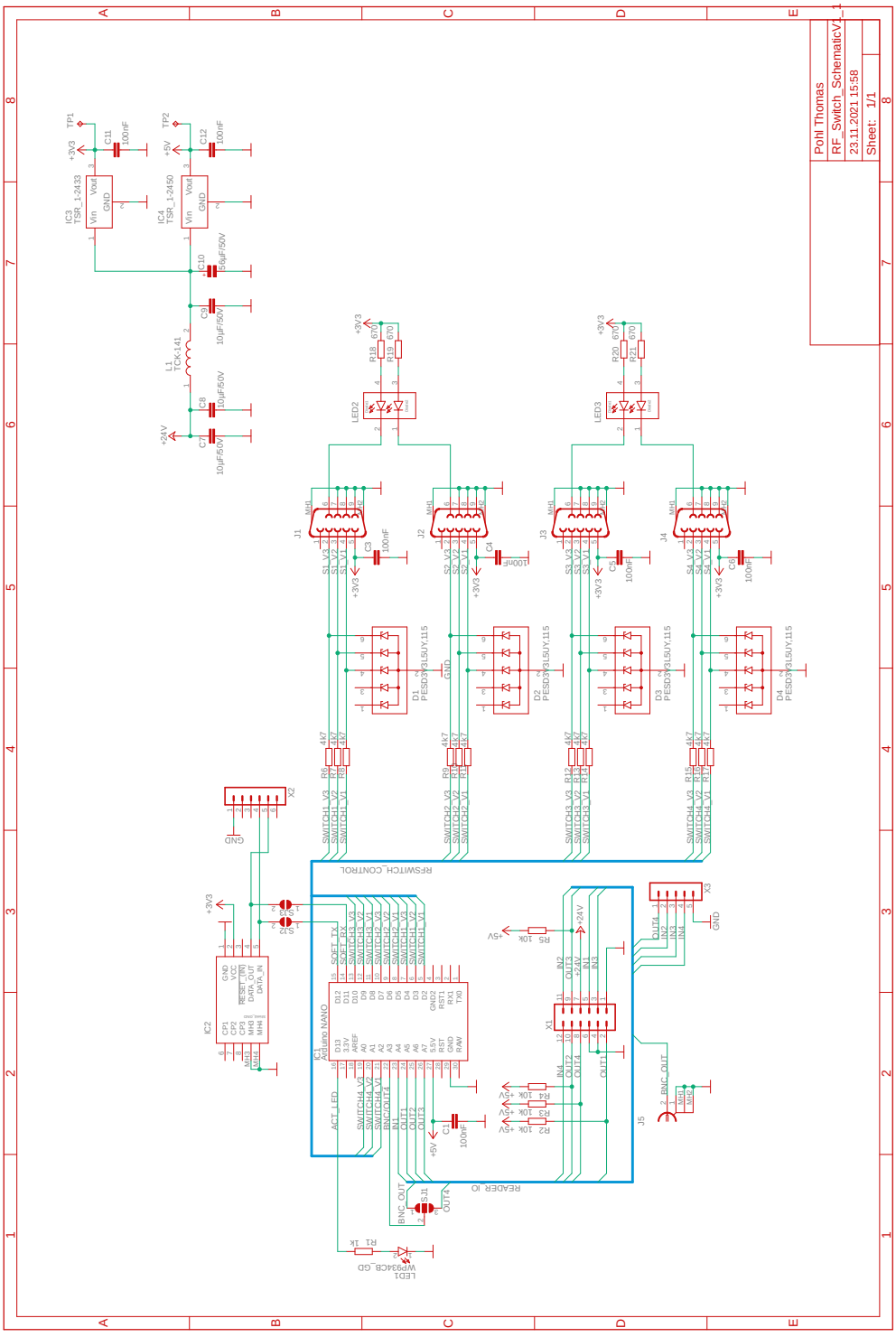

B Controller PCB Design

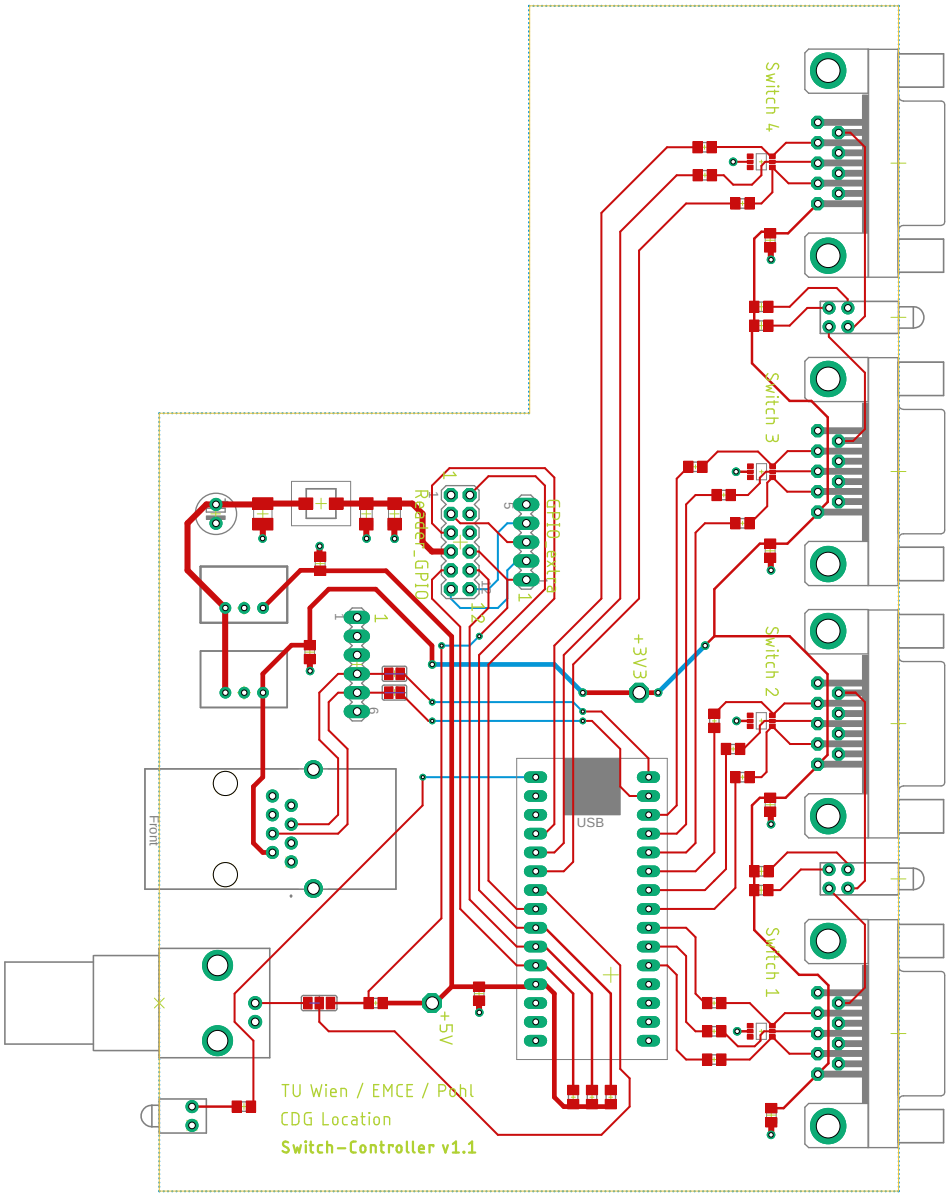

C Matlab Interface Guide

This appendix section gives a "How-To" guide to operating the measurement platform. After setting up the hardware, one needs to start a Matlab session and the corresponding GUI for the system. The first window (Fig. C.1a) shows the master screen for the main operation. The system has some predefined settings, but it is convenient to check them and make necessary changes, accessible by the button with the gear symbol. Fig. C.1b shows the settings window, where the user can set the communication profile, the initial Q, the used channels, and the transmit power for each of the four antenna ports on the reader. Changes can be saved or discarded by the corresponding button. These settings are held in the basic workspace of the Matlab session.

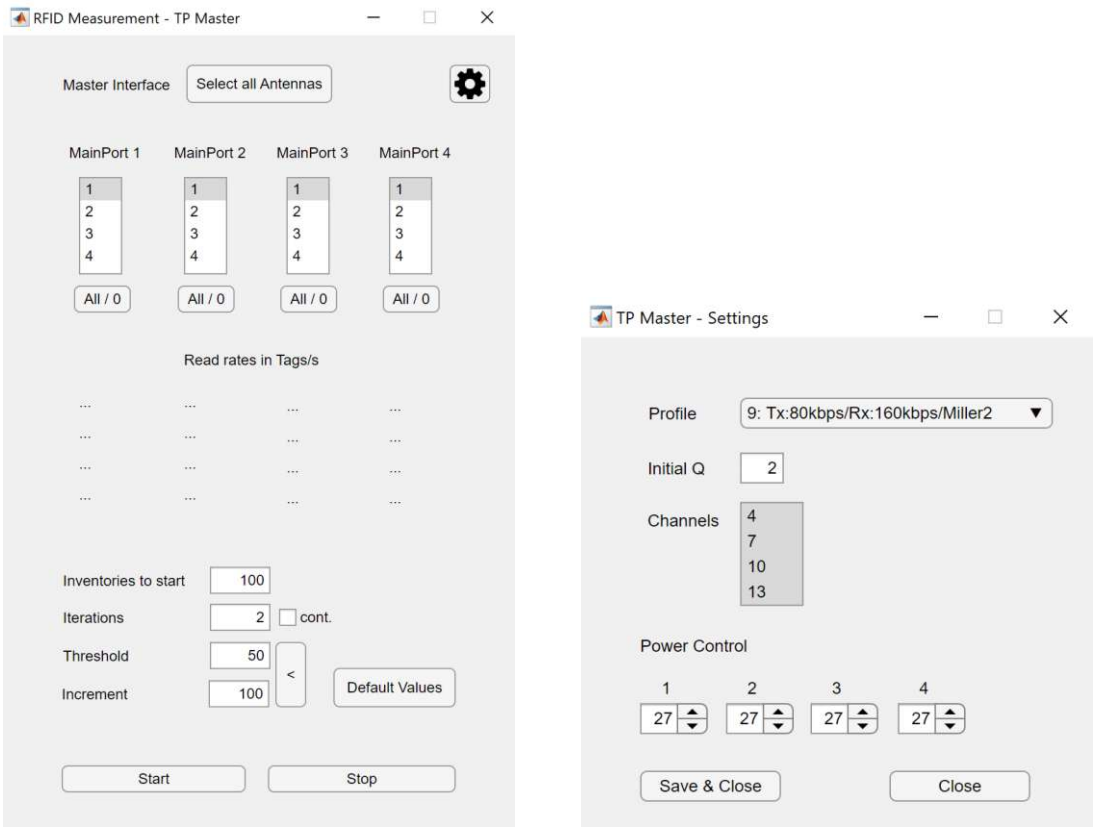

(a) **(b)**

Figure C.1: Matlab Interface a) Main Screen, b) Settings

After the preparation of all settings, one can select any needed antenna configuration in Fig. C.1a. Each main port represents a connector on the RFID reader unit. The sub ports are the selectable fields (1-4) for each main port. Multiple antennas can be selected by holding the "Ctrl" key and clicking on the desired ports. The following fields, which are dotted at the first start, will display the read rates for each antenna after the first process.

The values in the following four fields are essential for smooth operation. The first field "Inventories to start" takes the number of the first batch of inventories that are sent in the first sequence. Do not start with a small value to prevent idle times in the reader unit. A value of ≤ 100 seemed to be feasible. The next field "Iterations" takes the number of iterations so that the interface keeps on resending new batches of inventories. The third field "Threshold" sets the threshold to resend if the counter for the decoded frames for the current batch falls below. The fourth value field "Increment" specifies the number of inventory commands sent in each subsequent batch from the start sequence. Since sending commands to the reader via Ethernet is much faster than the reader takes to scan for tags, this process prevents the reader from falling into an idle process during a measurement campaign. If one does not know the exact time limit for the planned measurement, click on the continuous button, and the fields iteration, threshold, and increment will be disabled. This keeps the reader automatically on air until the stop button is pressed. By pressing the stop button, the software will stop sending another batch of inventories and finish decoding the commands sent so far. A click on the start button starts the process as the block diagram in Appendix D describes it.

The finished interface automatically cancels the connection to the reader and controller at the end. The received tag answers and their corresponding values are saved to the basic workspace of the current Matlab session, which can be used for further evaluation. Fig. C.2 shows a sample output of the tag data from the interface.

	EPC	Frequency	Phase	RSSI_dBm	NewTime	MaiP	SubP
1	"E200 4BA4 F34D 6B31 56A7 85AC"	865700	-151.8000	-84.3500	"12-07-2022 15:22:18.462"	1	2
2	"E200 4BA4 F34D 6B31 56A7 85AC"	867500	-230.6000	-78.3300	"12-07-2022 15:22:18.476"	2	2
3	"E200 4BA4 F34D 6B31 56A7 85AC"	866900	-151.8000	-83.7500	"12-07-2022 15:22:18.495"	3	2
4	"E200 4BA4 F34D 6B31 56A7 85AC"	866900	-5.6000	-84.3500	"12-07-2022 15:22:18.523"	1	2
5	"E200 4BA4 F34D 6B31 56A7 85AC"	865700	-247.4000	-79.6700	"12-07-2022 15:22:18.538"	2	2
6	"E200 4BA4 F34D 6B31 56A7 85AC"	866300	-50.6000	-84.9900	"12-07-2022 15:22:18.552"	3	2
7	"E200 4BA4 F34D 6B31 56A7 85AC"	866300	-258.6000	-84.9900	"12-07-2022 15:22:18.580"	1	2
8	"E200 4BA4 F34D 6B31 56A7 85AC"	867500	-208	-78.3300	"12-07-2022 15:22:18.595"	2	2
9	"E200 4BA4 F34D 6B31 56A7 85AC"	866300	-50.6000	-83.7500	"12-07-2022 15:22:18.610"	3	2
10	"E200 4BA4 F34D 6B31 56A7 85AC"	865700	-129.2000	-84.9900	"12-07-2022 15:22:18.638"	1	2

Figure C.2: Sample output of the interface

D Operation Sequence for the Measurement Platform

This appendix section gives a block diagram in Fig. D.3 with a brief description of the controller synchronization with the Matlab interface. The threshold for sending the next batch of inventory commands to the reader can be set in the Matlab interface software and can be stopped in continuous operation mode. A detailed "How-To" guide for operation is provided in Appendix C.

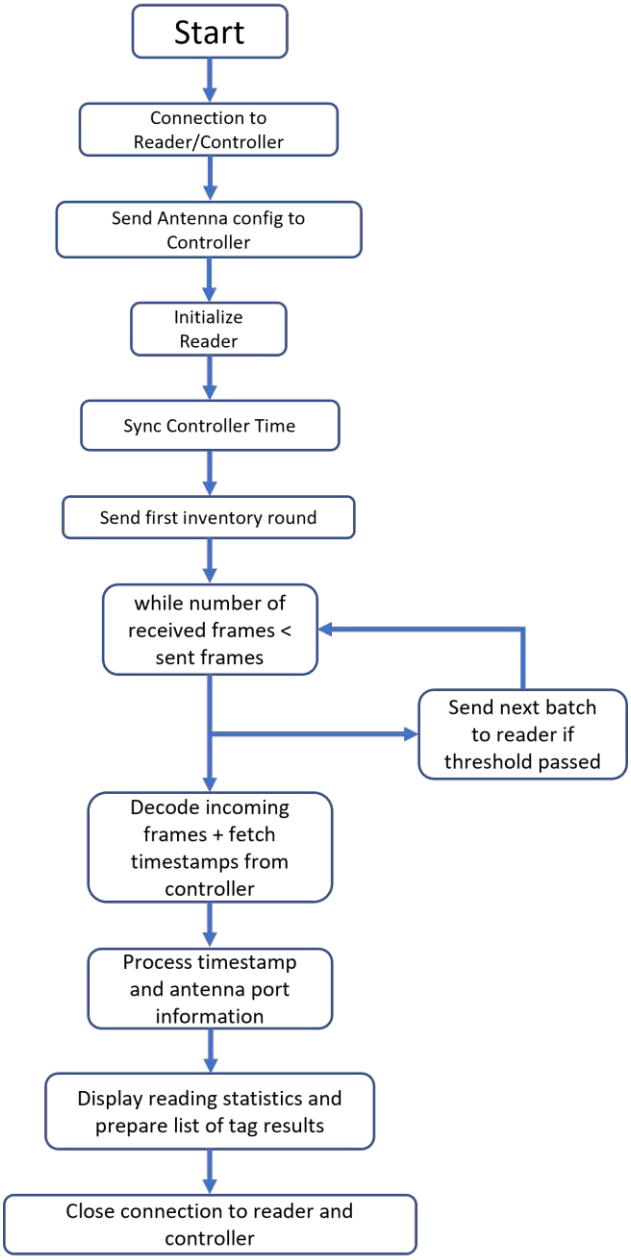

Figure D.3: Sequence diagram for the operation of the measurement platform

E Laser Ranger and PowerCube Control

This appendix section briefly describes the control of the laser ranger with the PowerCube. The PowerCube in this configuration (Fig. E.4a) can be moved in 2 rotatable axes. The construction is mounted upside-down to be able to move in azimuth and elevation. The construction to precisely align the laser in all axes from Fig. 4.12 is placed on the top, holding the laser-ranging device. This laser ranger can be controlled via a serial port connection. Since the PowerCube modules are controlled by a CAN-bus, I built a gateway consisting of an Arduino with a CAN-bus shield. The Arduino acts here as a gateway between the computer and the CAN controlled PowerCube modules. To make manual movements possible, the gateway has a "jog-only" mode, where the operator can control the PowerCube modules (azimuth and elevation) with the jog and the laser ranger to trigger the distance measurement with the button on the top of the jog. Fig. E.4b shows the control unit, including the gateway. The front consists of the power supply connection (24 V/3 A) for the motors and a USB connection for serial port control. Additionally, there is the power supply connector for the Arduino board, which is currently not used. For both the laser ranger and the PowerCube, I wrote a Matlab class to ensure easy control over two serial connections.

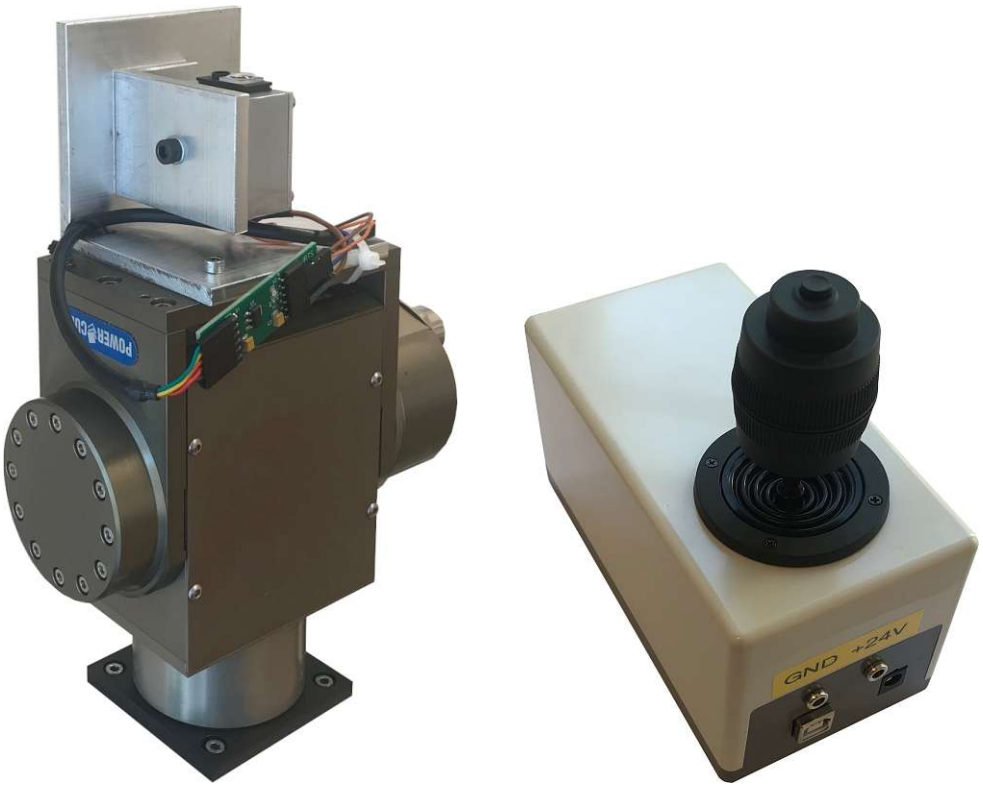

(a) **(b)**

Figure E.4: PowerCube with Control unit

Matlab control of the laser ranger (class: laserranger):
Create an object “LR” for the laser ranger: (COM port x and baud rate)

```
LR = laserranger('COMx', 19200);
```

Turn laser on/off:

```
LR.setLaser(s); % s = 1 (On), s = 0 (Off)
```

Measure distance: (returns distance in meters)

```
distance = LR.measureDistance();
```

Measure module temperature and power supply voltage:

```
result = getTemperature_and_PSV();
```

Matlab control of the PowerCube via gateway (class: powercube):
Create an object “PC” for the PowerCube: (COM port x and baud rate)

```
PC = powercube('COMx', 19200);
```

Set the operation mode of the gateway:
'P' - position mode, control via MATLAB, jog disabled
'J' - jog mode, jog enabled

```
PC.setMode('P');
```

Move PowerCube in position mode: (values in deg)

```
PC.Move(azimuth, elevation);
```

Get position from PowerCube: (values in deg)
Format is ...(azimuth, elevation)

```
Position = PC.GetPosition();
```

Hiermit erkläre ich, dass die vorliegende Arbeit gemäß dem Code of Conduct – Regeln zur Sicherung guter wissenschaftlicher Praxis (in der aktuellen Fassung des jeweiligen Mitteilungsblattes der TU Wien), insbesondere ohne unzulässige Hilfe Dritter und ohne Benutzung anderer als der angegebenen Hilfsmittel, angefertigt wurde. Die aus anderen Quellen direkt oder indirekt übernommenen Daten und Konzepte sind unter Angabe der Quelle gekennzeichnet.
Die Arbeit wurde bisher weder im In– noch im Ausland in gleicher oder in ähnlicher Form in anderen Prüfungsverfahren vorgelegt.

Wien, 24. August 2022 *Thomas Michael Pohl*